White Rose Research Online

eprints@whiterose.ac.uk
https://eprints.whiterose.ac.uk
Universities of Leeds, Sheffield and York

Deposited via The University of Leeds.

White Rose Research Online URL for this paper:
https://eprints.whiterose.ac.uk/id/eprint/247942/

Version: Accepted Version

Article:
Zhu, Y., Li, K. and Zhang, L. (2026) Stacked-Ensemble Forecasting for Resilient Operation of Base Station Microgrids Under Communication Failures. IEEE Internet of Things Journal. ISSN: 2327-4662

https://doi.org/10.1109/jiot.2026.3752576

This is an author produced version of an article published in Transportation Research Part C: Emerging Technologies, made available via the University of Leeds Research Outputs Policy under the terms of the Creative Commons Attribution License (CC-BY), which permits unrestricted use, distribution and reproduction in any medium, provided the original work is properly cited.

Reuse
This article is distributed under the terms of the Creative Commons Attribution (CC BY) licence. This licence allows you to distribute, remix, tweak, and build upon the work, even commercially, as long as you credit the authors for the original work. More information and the full terms of the licence here: https://creativecommons.org/licenses/

Takedown
If you consider content in White Rose Research Online to be in breach of UK law, please notify us by emailing eprints@whiterose.ac.uk including the URL of the record and the reason for the withdrawal request.

UNIVERSITY OF LEEDS
University of Sheffield
UNIVERSITY of York

Stacked-Ensemble Forecasting for Resilient Operation of Base Station Microgrids Under Communication Failures

Yingqi Zhu, *Student Member, IEEE*, Kang Li, *Senior Member, IEEE*, and Li Zhang, *Senior Member, IEEE*

***Abstract*—The resilient and economical operation of cellular base station microgrids (BSMGs) depends critically on accurate forecasting of renewable generation and load, particularly under communication link failures that disrupt real-time data exchange. However, forecasting model performance varies significantly with the underlying stability characteristics of historical datasets—a factor rarely considered in existing BSMG studies. This paper addresses this gap by proposing a stacked-ensemble forecasting framework that first assesses dataset stability and then guides model selection accordingly. Five complementary metrics, namely the augmented Dickey–Fuller (ADF) test, seasonal strength, approximate entropy (ApEn), the Hurst exponent, and trend-to-residual variance ratio (TRVR), are employed to characterize the stability, periodicity, and randomness of each dataset. These heterogeneous indicators are integrated into a unified stability score using grey relational analysis (GRA) enhanced by the entropy weight method (EWM), criteria importance through inter-criteria correlation (CRITIC), and the triangular fuzzy analytic hierarchy process (TF-AHP). Based on the resulting stability tier, a four-layer ensemble pool comprising three statistical models, three machine learning (ML) algorithms, two deep learning (DL) architectures, and two reinforcement learning (RL) schemes is selectively assembled. A random forest (RF) stacking model fuses their outputs to maximize forecast accuracy while maintaining low complexity. Simulation results demonstrate that the proposed stability-guided approach reduces weekday median root mean square error (RMSE) by 18.5% and improves median coefficient of determination (R^2) by 16.9% compared to baseline methods. Under two-link and three-link communication failure scenarios, the RF-Stacking-enabled dispatch reduces fault-induced transaction cost surges by approximately 15% and up to 40%, respectively. These findings confirm that systematically linking data stability assessment to ensemble model selection enhances both forecasting accuracy and operational resilience in communication-constrained BSMG environments.**

***Index Terms*—Base station microgrids, stacked ensemble forecasting, machine learning, random forest, dataset stability assessment.**

I. INTRODUCTION

In recent years, the rapid deployment of 5G networks, coupled with the explosive growth of Internet of Things (IoT) applications, has significantly increased the energy consumption and operational costs of cellular base stations (BSs). Integrating microgrids with cellular BSs is therefore becoming a rapidly growing trend, offering substantial benefits in terms of reliability, cost savings, sustainability, and network expansion [1]-[4]. While large-scale integration of renewable generation into these microgrids provides green power, it also introduces volatility and intermittency [5]-[7]. Across different time partitions and scenarios, generation and communication traffic load characteristics vary markedly, and no single metric can fully capture a dataset's stationarity, periodicity, and complexity. Critically, communication link failures can invalidate optimal trading schedules, leading to random reallocation of a faulty node's energy trades to other nodes or to the main grid, thereby significantly increasing overall trading costs [8]-[11]. Therefore, a forecasting-driven energy management approach that integrates multidimensional data with tiered model selection is essential for achieving accurate renewable power generation and communication load forecasting, resilient energy dispatch, computational efficiency, and fault tolerance.

Although various forecasting and control methods have been proposed for microgrid energy management, most existing approaches rely on a fixed pool of models without systematically evaluating the stability, periodicity, or randomness of the underlying data [12]-[15]. This rigidity limits their adaptability to heterogeneous datasets, often degrading prediction accuracy under fluctuating or nonstationary conditions, a limitation that becomes critical when communication link failures disrupt real-time data exchange. Existing dispatch frameworks commonly employ a sequential two-stage process of forecasting followed by optimization, which increases computational latency and reduces responsiveness in real-time operation. Furthermore, while the impact of communication failures on distributed energy systems has been widely acknowledged, few studies have quantitatively evaluated the additional transaction costs induced by such failures or investigated how data-driven forecasting mechanisms could mitigate these effects [16]-[18]. These gaps highlight the need for a unified, adaptive, and fault-resilient framework that first characterizes dataset stability using complementary metrics, then guides model selection via an enhanced multi-criteria ranking approach, and finally fuses selected models through a stacked ensemble to maintain forecasting accuracy and operational stability under communication failures.

The authors are with the School of Electronic and Electrical Engineering, University of Leeds, LS2 9JT Leeds, U.K. (e-mail: elyzhu@leeds.ac.uk, k.li1@leeds.ac.uk, l.x.zhang@leeds.ac.uk).

In response to these challenges, this study develops a stacked-ensemble forecasting-based energy management framework tailored for 5G-enabled cellular base station microgrids (BSMGs). The framework integrates a multi-criteria analysis approach to characterize heterogeneous renewable generation and communication traffic load datasets and guide adaptive model selection. Building on this foundation, a hierarchical ensemble forecasting method is designed to combine the strengths of different learning paradigms through a stacking-based integration strategy, thereby enhancing prediction robustness and generalization across varying operating conditions. Moreover, fault-aware transaction-cost models are constructed to quantify the economic impacts of communication link failures and evaluate the resilience of energy trading among interconnected BSMGs. Overall, the proposed approach aims to achieve accurate forecasting, fault-tolerant dispatch, and cost-efficient coordination in next-generation 5G-enabled microgrids, offering a unified perspective on the coupling between communication reliability and intelligent energy management.

The main contributions of this paper are summarized as follows:

1) A multidimensional dataset characterization framework is developed to capture the statistical, temporal, and stochastic properties of renewable generation and communication traffic load time-series data. The proposed scheme combines five stability indicators, namely the augmented Dickey–Fuller (ADF) test, seasonal strength (SS), approximate entropy (ApEn), Hurst exponent (H), and trend-to-residual variance ratio (TRVR), to quantitatively evaluate dataset stationarity and variability, thereby providing a robust foundation for adaptive model selection. The case study shows that using all five metrics improves median root mean square error (RMSE) by 18.5% and median coefficient of determination (R^2) by 16.9% compared to relying on only three metrics, which misclassifies stability and degrades forecast accuracy.
2) A multi-criteria decision mechanism is proposed in which grey relational analysis (GRA) serves as the core ranking method, while the entropy weight method (EWM), criteria importance through inter-criteria correlation (CRITIC), and the triangular fuzzy analytic hierarchy process (TF-AHP) are employed to derive complementary weights and adjust indicator importance. This GRA-centered scheme produces objective dataset scores and classifications, enhances model adaptability across heterogeneous data regimes, and reduces computational redundancy through informed model selection.
3) An adaptive hierarchical ensemble forecasting structure is constructed, consisting of diverse statistical models, machine learning (ML) algorithms, deep learning (DL) architectures, and reinforcement learning (RL) schemes. A random forest (RF) stacking model integrates their outputs, effectively leveraging complementary model strengths to enhance forecasting accuracy, robustness, and generalization under variable operating conditions. The case study shows that the proposed tiered RF-Stacking ensemble achieves 14–53% lower RMSE and 3–20% higher R^2 than the best-performing single models across all temporal partitions, demonstrating superior robustness and adaptability to varying dataset stability conditions.
4) Fault-aware transaction-cost models are designed to analyze the economic impacts of communication link failures in dual- and triple-BS configurations. Through multi-scenario evaluation (annual, seasonal, weekday, and weekend datasets), the framework demonstrates that accurate forecasting and adaptive dispatch can significantly mitigate the additional costs caused by fault-driven trade reallocations. Quantitatively, the case study shows that across two-link and three-link disruption scenarios, the RF-Stacking-enabled dispatch reduces fault-induced transaction cost increases by approximately 15% and up to 40%, respectively, highlighting the resilience benefits of accurate forecasting under communication failures.

The rest of the paper is organized as follows: Section II reviews the related work. In Section III, data-driven decision support framework is explained. The forecasting models are described in Section IV. In Section V, the case study and simulation results are presented. Finally, Section VI concludes the paper.

II. RELATED WORKS

Recent research on microgrid energy management has increasingly focused on improving forecasting accuracy and dispatch efficiency through data-driven and optimization-based techniques. These methods aim to enhance renewable energy utilization, reduce operational costs, and support coordinated control among distributed nodes. Yan et al. [19] introduced a software-defined networking (SDN)–based energy trading method using the nonlinear tangent perturbation–multiagent proximal policy optimization (NTP-MAPPO) algorithm to enhance renewable utilization and trading efficiency across cellular BSMGs. Their work demonstrated the potential of combining network programmability with RL to achieve adaptive and cooperative energy transactions. Bao et al. [20] proposed a cooperative game–based dispatch framework that integrates 5G BSs and energy storage (ES) systems into a virtual power plant using an improved random drift particle swarm optimization (PSO) algorithm, achieving balanced power allocation and improved system reliability. Surathunmanun et al. [21] proposed a short-term photovoltaic (PV) forecasting framework for sensor-constrained microgrids using cloud top temperature imagery and Vision Transformer models, which significantly improved forecasting accuracy, yet its design was mainly oriented toward single-site prediction and offered limited support for multi-node energy management and trading-oriented decision-making. Overall, these studies have significantly advanced the optimization and forecasting capabilities of microgrids. However, most rely on a fixed model pool and overlook the influence of data heterogeneity, dynamic uncertainty, and temporal stability on model selection and performance robustness, gaps that become particularly critical when communication link failures disrupt real-time data exchange and when dataset stability characteristics vary

markedly across different time partitions and scenarios.

In parallel, several studies have investigated energy management and forecasting under communication constraints or link failures, aiming to preserve operational stability within distributed microgrid networks. Zhou et al. [22] proposed a multiagent Bayesian deep reinforcement learning (BA-DRL) framework for microgrid energy management in the presence of communication disruptions. Their method enhanced cooperative decision-making among agents through probabilistic inference but was not validated across datasets with diverse temporal and statistical characteristics. Arbab-Zavar et al. [23] applied DL techniques to forecast next-step generation and consumption, seeking to reduce control disruptions and improve system responsiveness during link failures. Although their results showed improved short-term prediction accuracy, they did not quantify or compare the actual reductions in loss or trading cost achieved through these forecasts. Zhang et al. [24] proposed a coordinated scheduling strategy that leverages the flexible load management capability of 5G BSs to optimize microgrid operations. While their approach demonstrated improvements in power allocation and renewable utilization, it did not explicitly consider link reliability or fault-induced communication delays. Overall, these studies provide valuable insights into the interaction between communication reliability and microgrid control. However, they often focus primarily on control stability rather than transaction-level economic effects, and few have quantified the cost surges or evaluated the role of predictive resilience in mitigating failure-induced performance degradation.

Recent advances in power and energy time-series forecasting have produced a range of adaptive and hybrid DL architectures. For example, Rahmatinia et al. [25] proposed convolutional–long short-term memory transformer (CLM-Former) for multi-horizon smart microgrid forecasting, integrating time-series decomposition, autocorrelation-based attention, and convolutional–recurrent subnetworks to jointly capture seasonal dependencies and short-term variations. Peng et al. [26] developed an adaptive deep forecasting framework based on an improved African vulture optimization algorithm (IAVOA) and an efficient attention temporal convolutional network (EATCN), where decomposition, attention mechanisms, and parameter optimization are jointly employed to enhance prediction accuracy. Qiu et al. [27] introduced a hybrid model combining complete ensemble empirical mode decomposition with adaptive noise (CEEMDAN), an improved sparrow search algorithm (ISSA), a convolutional neural network (CNN), and bidirectional long short-term memory (BiLSTM) to address nonlinearity and nonstationarity in energy time-series patterns. Chen et al. [28] presented a dual-channel multi-scale long short-term memory (DCMS-LSTM) model with wavelet decomposition and cross-channel attention for real-world short-term power forecasting. While these approaches enhance adaptivity within predefined architectural frameworks, through decomposition, attention mechanisms, optimization-based tuning, or multi-scale feature extraction. Yet, they do not address adaptivity at the dataset level. This paper instead focuses on dataset-level adaptivity: prior to constructing the stacked ensemble, the statistical and temporal characteristics of each data partition are evaluated to determine the appropriate model-complexity tier. This strategy avoids unnecessary model complexity for stable datasets while preserving more flexible model pools for volatile ones, thereby tailoring the forecasting framework to the intrinsic characteristics of the data itself.

Despite these advances, several gaps remain. First, most existing studies improve forecasting accuracy through a fixed or predefined model structure, while the connection between dataset characteristics and model-complexity selection is still insufficiently explored. Second, although communication-constrained microgrid operation has received increasing attention, few studies have quantitatively evaluated how communication-link unavailability affects transaction-level costs in interconnected BSMGs. Third, the role of forecasting accuracy in mitigating communication-induced cost increases has not been fully investigated. These limitations motivate this work, which develops a stability-guided forecasting-driven energy management framework that integrates: (i) five complementary metrics (ADF, SS, ApEn, H, TRVR) for multidimensional dataset evaluation; (ii) an enhanced GRA-based multi-criteria ranking (EWM, CRITIC, TF-AHP) for adaptive tiered model selection; (iii) a four-layer RF-Stacking ensemble (statistical, ML, DL, RL) for robust forecasting; and (iv) fault-aware dispatch optimization that reduces transaction cost surges under communication failures, thereby enabling resilient and efficient BSMG operations.

III. Data-driven Decision Support Framework

A. Flowchart of the Proposed Methodology

To clearly illustrate the logical framework of the proposed study, the overall flowchart is presented in Fig. 1. The process is organized into five sequential stages, as outlined below.

Stage 1: Dataset Characterization – The process begins with the extraction and analysis of statistical, temporal, and complexity attributes from wind, PV, and communication traffic load datasets. Five complementary metrics — namely the ADF test, SS, ApEn, H, and TRVR — are employed to quantitatively evaluate dataset stability, periodicity, and randomness.

Stage 2: Multi-Criteria Decision Making – A multi-criteria decision-making mechanism is then applied to comprehensively score and classify the datasets. This stage integrates one subjective weighting scheme (TF-AHP) and two objective weighting schemes (EWM and CRITIC) within an enhanced GRA framework. The resulting stability score guides adaptive model selection in the subsequent stage.

Stage 3: First-Level Base Model Ensemble – Based on the dataset stability classification, a first-level ensemble of base forecasting models is trained to capture heterogeneous temporal structures and nonlinear dependencies. The base model pool comprises three statistical methods, three ML algorithms, two DL architectures, and two RL schemes, ensuring broad coverage of learning paradigms.

Stage 4: Second-Level Stacked Ensemble (RF-Stacking) – The outputs of all base learners are then integrated through a second-level stacking model implemented via the RF algorithm. This stacked ensemble enhances forecasting accuracy,

robustness, and generalization across heterogeneous and nonstationary data scenarios.

Stage 5: Fault-Aware Economic Assessment – Finally, transaction cost models are developed to evaluate the proposed framework's resilience and economic performance under communication link failures. By simulating dual-link and triple-link fault scenarios among cellular base stations, the impact of communication disruptions on energy trading and dispatch costs is quantitatively analyzed, with performance measured against baseline methods.

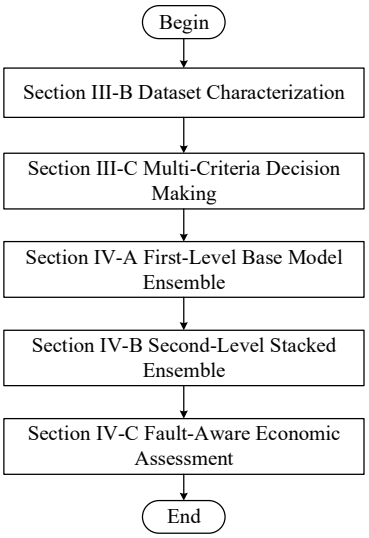


Fig. 1. Flowchart of the proposed methodology.

B. Data and feature analysis

Time-series data in microgrid applications typically exhibit mixed characteristics arising from variability of renewable generation, communication traffic load dynamics, and inherent wireless communication uncertainties. These patterns can generally be decomposed into trend, seasonality, and random noise, each influencing forecasting performance in distinct ways [29]. To objectively assess data properties and guide model selection, five complementary statistical indicators are employed. Together, they quantify stationarity, periodicity, complexity, long-term dependency, and signal quality, providing a multi-perspective understanding of dataset behavior. This multidimensional characterization helps identify whether a dataset favors linear, seasonal, or nonlinear models, and determines the need for detrending, denoising, or advanced learning architectures.

1) ADF p-value

The ADF test evaluates the stationarity of a time series by testing the null hypothesis that the series contains a unit root. A high ADF p-value indicates non-stationarity, suggesting the presence of persistent trends or drifts, whereas a low p-value implies that the mean and variance remain stable over time. The ADF result can guide whether differencing or detrending should be performed before model training [30]. The original model for the ADF test is

$$\Delta x_t = \alpha + \beta t + \gamma x_{t-1} + \sum_{i=1}^{p-1} \phi_i \Delta x_{t-i} + \varepsilon_t \tag{1}$$

$$\mathrm{ADF_stat} = \hat{\gamma} \Big/ \mathrm{SE}(\hat{\gamma}) \tag{2}$$

where x_t is the original time series at time t, α is the intercept term, β is the time-trend coefficient, γ is the autoregressive coefficient, p is the number of lagged differences with coefficients ϕ_i, ε_t is the random error term, $\hat{\gamma}$ is the estimator of γ, $\mathrm{SE}(\hat{\gamma})$ is the standard error of $\hat{\gamma}$, and ADF_stat is the resulting test statistic.

2) SS

SS quantifies the proportion of variance explained by the seasonal component after decomposition, typically obtained from a seasonal–trend decomposition based on Loess (STL). A higher SS value indicates a pronounced periodic pattern, implying that models incorporating explicit seasonal structures are more appropriate. Conversely, a low SS value suggests irregular or weak seasonality, favoring non-seasonal or adaptive methods [31].

$$x_t = s_t + t_t + r_t \tag{3}$$

$$\mathrm{SS} = \frac{\mathrm{Var}(s_t)}{\mathrm{Var}(x_t)} \tag{4}$$

where s_t, t_t and r_t denote the seasonal component, trend component and remainder component respectively, and $\mathrm{Var}(\cdot)$ is the variance operator.

3) ApEn

ApEn measures the complexity and unpredictability of a time series. It quantifies the likelihood that similar patterns remain similar on subsequent observations. A low ApEn value implies high regularity and deterministic behavior, while a high ApEn value reflects randomness or chaotic fluctuations. Datasets with high ApEn typically benefit from nonlinear or black-box learning models, which can capture complex temporal dependencies beyond traditional statistical approaches [32].

$$\phi(m) = \frac{1}{N-m+1} \sum_{i=1}^{N-m+1} \ln[C_i^m(r)] \tag{5}$$

$$C_i^m(r) = \frac{1}{N-m+1} \sum_{j=1}^{N-m+1} 1\left\{ \max_{0 \leqslant k < m} \left| x_{i+k} - x_{j+k} \right| \leqslant r \right\} \tag{6}$$

$$\mathrm{ApEn}(m,r) = \phi(m) - \phi(m+1) \tag{7}$$

where N is series length, m is the embedding dimension, r is the distance-tolerance threshold, $1\{\cdot\}$ is the indicator function, $\phi(m)$ is the mean log-match rate, and ApEn denotes the approximate entropy.

4) H

The H assesses the long-memory and mean-reversion characteristics of a series. Values of H>0.5 indicate persistence where increases tend to be followed by further increases, while H<0.5 suggests anti-persistence or mean reversion. A value of H close to 0.5 denotes a random walk. This metric provides insight into whether trend-following, mean-reverting, or purely stochastic models are more suitable, offering a valuable perspective for selecting models sensitive to long-term temporal dependence [33].

$$Y_k = \sum_{t=1}^{k} (x_t - \bar{x}), k = 1, 2, \cdots, N \tag{8}$$

$$R = \max_{1 \leqslant k \leqslant N} Y_k - \min_{1 \leqslant k \leqslant N} Y_k \tag{9}$$

$$S = \sqrt{\frac{1}{N}\sum_{t=1}^{N}(x_t - \bar{x})^2} \tag{10}$$

$$\mathrm{H} = \frac{\ln(R/S)}{\ln N} \tag{11}$$

where $\bar{x}$ is the series mean, Y_k is the demeaned cumulative sum, R is the range (maximum minus minimum), and S is the sample standard deviation.

5) TRVR

The TRVR is employed in this study as a statistical data-quality indicator to characterize the relative dominance of systematic temporal variation over irregular residual fluctuations in a decomposed time series. After seasonal–trend decomposition using a locally estimated scatterplot smoothing (LOESS) approach, TRVR is calculated as the ratio of the variance of the trend component to that of the residual component:

$$\mathrm{TRVR} = \frac{\mathrm{Var}(t_t)}{\mathrm{Var}(r_t)} \tag{12}$$

A higher TRVR indicates that the time series is dominated by a clear and systematic trend component, suggesting stronger temporal regularity and higher predictability. In such cases, simpler forecasting models, such as statistical or linear methods, may be sufficient to capture the underlying dynamics. Conversely, a lower TRVR indicates that residual fluctuations or stochastic disturbances are more dominant, implying greater temporal irregularity and potentially higher forecasting difficulty. These datasets typically require more flexible and higher-capacity models, such as ML, DL, or RL-based predictors, to adequately capture the underlying patterns.

Thus, TRVR provides a quantitative, data-driven measure of the clarity and predictability of temporal dynamics. By characterizing the relative dominance of systematic variation over irregular fluctuations, TRVR supports the selection of an appropriate level of model complexity for reliable forecasting, ensuring that computational resources are allocated in proportion to the inherent modeling difficulty of each dataset [34].

C. Scoring Mechanism for Decision Support

The five evaluation metrics introduced in Section III-B emphasize different data characteristics. Some datasets may exhibit strong stationarity or periodicity but weak complexity or low TRVR, while time series with long-memory behavior may also show high entropy or pronounced noise. As a result, no single metric can adequately capture the diverse properties of all datasets, and relying on individual metrics or simple averaging may lead to inappropriate model-tier assignment.

To address this issue, we adopt an integrated GRA-based decision model that combines subjective TF-AHP with objective EWM and CRITIC weighting. By jointly considering stationarity, periodicity, complexity, long-memory behavior, and noise level, the proposed scoring mechanism yields an interpretable dataset-level score for adaptive model selection. Compared with a learnable gating strategy, this design is more suitable for the present setting because model selection is performed at the dataset level, where only a limited number of representative data partitions are available. Under such conditions, the proposed multi-criteria mechanism remains transparent, computationally lightweight, and less prone to overfitting. In this way, sequences with lower scores are matched with more flexible nonlinear models, whereas higher-scoring sequences are assigned simpler models, enabling adaptive forecasting across heterogeneous data scenarios.

1) TF-AHP

TF-AHP applies triangular fuzzy numbers to capture subjectivity and uncertainty in multi-criteria evaluation. Fuzzy comprehensive evaluation offers a rigorous and streamlined method to simplify and quantify multi-criteria dataset scoring [35]. The evaluation framework employs a consistent set of five indicators across all datasets. These indicators constitute the indicator layer and collectively inform the overall evaluation measure in the target layer. As shown in Fig. 2, the blue-shaded box represents the top-level evaluation objective, while the orange boxes denote the shared assessment criteria.

To derive the indicator weights required by TF-AHP, the normalized weight of the i-th indicator is computed as

$$r_i = \frac{\sum_{j=1}^{n} q_{ij}}{\sum_{k=1}^{n}\sum_{j=1}^{n} q_{kj}}, i = 1, 2, \cdots, n \tag{13}$$

where r_i is the weight of the i-th indicator, q_{ij} and q_{kj} are entries in i-th and k-th row individually of column j in the evaluation matrix, and n is the total number of indicators.

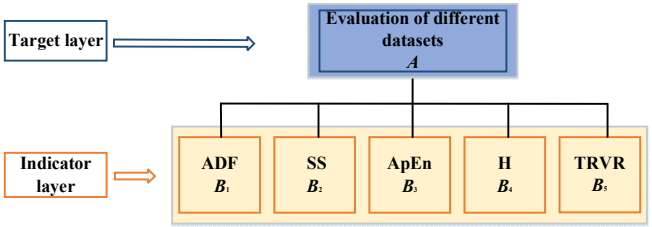


Fig. 2. The hierarchical structure of dataset assessment.

2) CRITIC

CRITIC is an objective weighting method that evaluates contrast by each indicator's standard deviation (higher deviations indicate a wider range of values) and conflict by inter-indicator correlations (stronger positive correlations denote lower conflict) [36].

Firstly, the original indicator values are forward-oriented and standardized to form matrix $b_{ij}^{'}$.

$$b_{ij}^{'} = \begin{cases} \dfrac{x^{\max}(j) - x_i(j)}{x^{\max}(j) - x^{\min}(j)}, \text{if indicator } j \text{ is negative} \\ \dfrac{x_{i_0}(j) - x^{\min}(j)}{x^{\max}(j) - x^{\min}(j)}, \text{if indicator } j \text{ is positive} \end{cases} \tag{14}$$

where $x_i(j)$ is the original value of indicator j, and $x^{\max}(j)$ and $x^{\min}(j)$ are maximum and minimum values of that indicator.

Secondly, calculate each indicator's information capacity.

$$\sigma_j = \sqrt{\frac{\sum_{i=1}^{m_0}(b_{ij}^{'} - \bar{x}_j)}{m_0 - 1}} \tag{15}$$

$$f_j = \sum_{i=1}^{m_0}(1-r_{ij}) \tag{16}$$

$$C_j = \sigma_j f_j \tag{17}$$

where $\bar{x}_j$ is the mean of indicator j, r_{ij} is the correlation coefficient between indicators i and j, m_0 is the number of samples, C_j is the information capacity, σ_j is the contrast, and f_j is the conflict.

Finally, calculate the weight ω_i of each indicator.

$$\omega_j = \frac{C_j}{\sum_{k=1}^{n} C_k}, j = 1,2,\cdots,n \tag{18}$$

3) EWM

EWM objectively weights indicators by their variability. Indicators with lower entropy convey more information and thus receive higher weights, whereas those with higher entropy convey less information and receive lower weights [37].

First, construct the probability matrix $P = \left[p_{ij}\right]_{m_0 \times n}$, where each element is computed as

$$p_{ij} = \frac{b_{ij}^{'}}{\sum_{i=1}^{m_0} b_{ij}^{'}} \tag{19}$$

Secondly, calculate each indicator's information entropy e_j and corresponding utility value d_j.

$$e_j = -\frac{1}{\ln m_0}\sum_{i=1}^{m_0} b_{ij}^{'} \ln b_{ij}^{'} \tag{20}$$

$$d_j = 1 - e_j \tag{21}$$

Finally, calculate the weight W_{j_0} of each indicator.

$$W_j = \frac{d_j}{\sum_{k=1}^{n} d_k}, j = 1,2,\cdots,n \tag{22}$$

4) GRA

GRA applies geometric measures to quantify each dataset's proximity to an ideal value, and smaller deviations indicate stronger alignment [38].

Compute the mean of the processed array x, derive each index's correlation coefficient, and then calculate the grey correlation degree. The formulas are given as follows:

$$x_i^{'}(j) = \frac{x_i(j)}{\bar{x}_j^{'}} \tag{23}$$

$$\zeta_i(j) = \frac{\Delta_{\min} + \rho\Delta_{\max}}{\Delta_i(j) + \rho\Delta_{\max}} \tag{24}$$

$$D = \frac{1}{m_0}\sum_{j=1}^{n}\zeta_i(j) \tag{25}$$

where $\zeta_i(j)$ is the correlation coefficient of the j-th indicator, $x_i^{'}(j)$ denotes the j-th indicator value of the ideal dataset, formed by the optimal values of all evaluation metrics, $\bar{x}_j^{'}$ is the average value, $\Delta_i(j) = \left|x_i(j) - x_i^{'}(j)\right|$, $\Delta_{\max} = \max_i \max_j \Delta_i(j)$, $\Delta_{\min} = \min_i \min_j \Delta_i(j)$, and ρ is the resolution coefficient, generally taken as 0.5.

5) Improved GRA

To capture the multifaceted impact of indicators on dataset evaluation, GRA combines TF–AHP, CRITIC, and EWM for an objective, holistic evaluation of each dataset. This framework facilitates optimal model selection, as illustrated in Fig. 3. Indicator weights from these models are averaged to obtain α_j. Eq. (25) is updated to the following grey relation formula:

$$D_0 = \sum_{j=1}^{n}\alpha_j\zeta_i(j) \tag{26}$$

where D_0 denotes the improved grey relational degree.

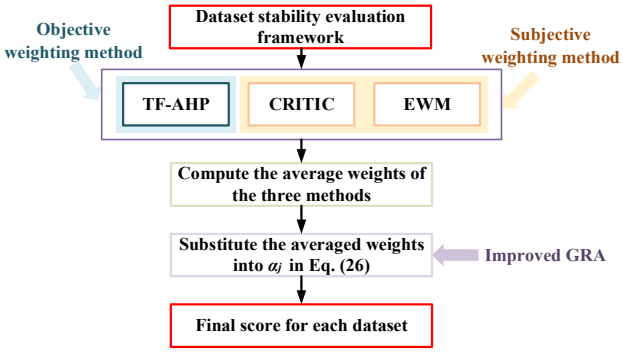


Fig. 3. Evaluation flowchart for each dataset.

IV. Base Models and Stacked Ensemble Structure

A. First-level base models

This study selects ten representative forecasting models spanning statistical analysis, ML, DL, and RL paradigms to construct a diverse and complementary first-level model pool. The characteristics and configurations of each base model are summarized in Table I.

TABLE I

Overview of First-level Base Models

Category	Models	Remarks
Statistical	Autoregressive integrated moving average (ARIMA) [41]	Effective for stationary, short-term series but assumes linearity and poor with volatile data.
	Seasonal ARIMA (SARIMA) [42]	Captures seasonality but is complex and tuning-sensitive.
	Prophet [43]	Automatically models trends, seasonality, holidays & events, but risks overfitting holiday effects.
ML	eXtreme gradient boosting (XGBoost) [44]	Fast and suitable for sparse data but sensitive to hyperparameters.
	Light gradient boosting machine (LightGBM) [45]	Very fast and memory-efficient but sensitive to categorical encoding.
	Categorical boosting (CatBoost) [46]	Natively supports categorical but slows on large datasets.
DL	Long short-term memory (LSTM) [47]	Captures long-term dependencies but is data-hungry and prone to vanishing gradients.
	Transformer [48]	Parallelizable but computationally expensive.
RL	Deep Q-network (DQN) [49]	Suitable for discrete actions but demands large replay memory.
	Proximal policy optimization (PPO) [50]	Stable updates but tuning-intensive and sample-inefficient.

Statistical models capture linear and seasonal dependencies, ML algorithms provide nonlinear mapping and interpretability, and DL architectures are effective for long-term temporal feature extraction. In addition, RL-based models, specifically DQN and PPO, are employed as complementary sequential predictors to learn adaptive prediction policies from dynamic time-series environments. Unlike conventional supervised learning models that minimize a static loss function, RL-based forecasters interact with the environment, receiving reward signals that guide the policy toward improved sequential prediction performance.

For example, Wu et al. [39] developed a DQN-based framework for short-term load and price forecasting by modeling the prediction process as a Markov decision process, where the action represents the predicted load and price, and the reward penalizes forecasting errors. Forecast-aware PPO has also been applied in energy scheduling by incorporating short-term demand and renewable-generation forecasts into the decision process [40].

Please note that in this study, DQN and PPO are not treated as conventional statistical forecasting models, but rather as RL-based candidate predictors within the first-level model pool. Their inclusion is motivated by the need to introduce prediction patterns and error structures that differ fundamentally from those of supervised learning models, an essential property for effective stacked ensemble learning.

For these RL-based predictors, the forecasting mechanism is defined as follows:

State: A rolling historical window of the target variable and relevant exogenous variables, including renewable generation, load demand, storage operation, grid exchange, and peer-to-peer (P2P) trading variables.

Action: The next-step prediction decision, expressed as a discretized correction to the baseline forecast.

Reward: Defined according to the negative forecasting error, with additional penalties for large deviations or infeasible predictions to encourage physically plausible outputs.

Training process: The agents interact with the historical time-series environment, updating their policies to maximize cumulative forecasting rewards. DQN employs experience replay and a target network for stable Q-learning, while PPO uses a clipped surrogate objective for stable policy updates.

Forecast-output mechanism: After training, the selected action is mapped back to a numerical forecast correction, which is added to the baseline value to generate the final DQN/PPO forecast output.

For implementation, both RL-based predictors use a 24-h historical input window and two fully connected hidden layers with 64 neurons per layer and rectified linear unit (ReLU) activation. The DQN predictor is trained using the Adam optimizer with a learning rate of 1×10^{-3}, a discount factor of 0.95, a minibatch size of 32, and a replay-buffer capacity of 20,000 samples. The PPO predictor uses Adam with a learning rate of 3×10^{-4}, a discount factor of 0.99, a minibatch size of 64, a clipping parameter of 0.2, and a generalized-advantage-estimation parameter of 0.95. These settings follow commonly adopted DQN/PPO configurations in energy-management applications [51], [52].

It should be noted that the resulting RL-based predictions are used as candidate inputs to the RF-Stacking ensemble, alongside the outputs of the statistical, ML, and DL base models. The inclusion of DQN and PPO provides adaptive candidate forecasts with prediction patterns and error structures that differ significantly from those of conventional supervised learning models. This diversity is a critical enabler of stacked ensemble learning, as it allows the RF-Stacking ensemble to:

1) Assign data-dependent importance to different forecasting paradigms.

2) Reduce dependence on any single base model.

3) Improve robustness and generalization across heterogeneous datasets and operating conditions.

By leveraging the complementary strengths of statistical, ML, DL, and RL-based forecasters, the proposed ensemble achieves a more balanced and resilient forecasting performance than any single paradigm could provide in isolation.

B. Second-level Stacking Model

The second-level stacking model integrates the outputs of the base models to capture their nonlinear complementarities. The RF regressor is adopted for its robustness against high-dimensional noise and its ensemble averaging mechanism that mitigates overfitting. The tree-based structure of the RF efficiently captures complex interactions among first-level predictions while requiring relatively few hyperparameters, thus simplifying ensemble optimization. The flowchart of the stacking model is shown in Fig. 4. The overall mapping relationship between base-model outputs and the final prediction is expressed as:

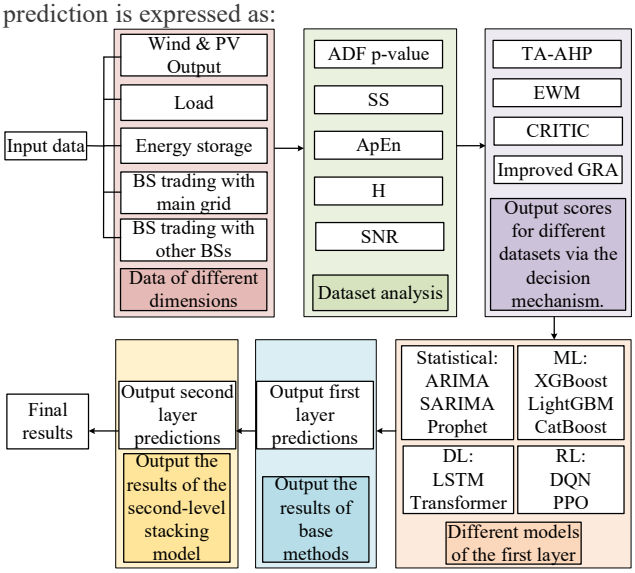


Fig. 4. Flowchart of RF-Stacking model.

To prevent information leakage and ensure a realistic assessment of the ensemble's generalization capability, the RF meta-learner is trained using a rolling-window out-of-fold (OOF) prediction procedure applied exclusively to the training and validation data. This approach is specifically designed to preserve the temporal order of the time-series data and to eliminate the risk of future information contaminating the meta-learner training process.

The procedure consists of the following steps:

1) Chronological fold division: The historical training and validation samples are partitioned into multiple chronological

folds while strictly preserving the temporal order of the time series.

2) OOF prediction generation: Starting from the second fold, the base models are trained on all preceding folds and then used to predict the current fold. This procedure is repeated sequentially for each subsequent fold, ensuring that each validation fold is predicted using only earlier data. Therefore, the temporal order is preserved and information leakage is avoided.

3) Meta-feature construction: The OOF predictions from all base models are concatenated to form the meta-feature vector for each sample. This vector serves as the input representation for training the RF meta-learner.

4) Meta-learner training: The RF meta-learner is trained on the meta-feature vectors using the corresponding true target values as labels, learning to optimally combine the base model predictions.

5) Final testing: After meta-learner training, all first-level base models are retrained using the complete training and validation data. Their predictions on the held-out test set are then fed into the trained RF meta-learner to produce the final ensemble forecasts.

This rolling-window OOF procedure ensures that the meta-learner is trained only on predictions generated from previously unseen validation samples, thereby preventing information leakage and preserving the temporal structure of the data.

$$z(x) = \left[\hat{y}_1(x), \hat{y}_2(x), \cdots, \hat{y}_{10}(x)\right] \tag{27}$$

$$\hat{y}(x) = F(z(x)) \tag{28}$$

where $\hat{y}_1(x), \hat{y}_2(x), \cdots, \hat{y}_{10}(x)$ denote the predicted outputs of the ten first-level base models, $z(x)$ represents the concatenated feature vector composed of these base-model outputs, $F(\cdot)$ is the second-level stacking mapping function, and $\hat{y}(x)$ denotes the final prediction obtained after stacking-based fusion.

To ensure that the predicted operation trajectories are physically and economically feasible, the following constraints are imposed. These include the power balance between load and generation, ES charging and discharging limits, and state-of-charge (SoC) consistency conditions.

1) Inequality constraints.

$$0 \le P_{t,dis} \le P_{t,dis}^{\max} \tag{29}$$

$$0 \le P_{t,ch} \le P_{t,ch}^{\max} \tag{30}$$

$$E_{BS}^{\min} \le E_s(t) \le E_{BS}^{\max} \tag{31}$$

$$E_{BS}^{\min} \le E_s(0) + \eta \sum_{t=1}^{T} [P_{t,ch}\Delta t] - \frac{1}{\eta} \sum_{t=1}^{T} [P_{t,dis}\Delta t] \le E_{BS}^{\max} \tag{32}$$

$$U_{t,dis} + U_{t,ch} \le 1 \tag{33}$$

where $P_{t,ch}^{\max}$ and $P_{t,dis}^{\max}$ are the ES's maximum charge and discharge power, T=24 h is the scheduling horizon, $E_s(0)$ is the initial capacity, $E_{BS}^{\max}$ and $E_{BS}^{\min}$ are the upper and lower capacity limits, $P_{t,dis}$ and $P_{t,ch}$ are the discharge and charging power at time t, η is the charging and discharging efficiency, $U_{t,dis}$ and $U_{t,ch}$ are binary variables representing the BSES operating state. Eq. (33) ensures that the ES cannot charge and discharge simultaneously, while allowing both states to reach zero when the system is idle.

2) Equality constraints.

$$\eta \sum_{t=1}^{T} [P_{t,ch}\Delta t] - \frac{1}{\eta} \sum_{t=1}^{T} [P_{t,dis}\Delta t] = 0 \tag{34}$$

$$E_s(t+1) = E_s(t) + \eta P_{t,ch}\Delta t - \frac{1}{\eta} P_{t,dis}\Delta t \tag{35}$$

$$\begin{aligned} &P_{pv}(t) + P_{pw}(t) + P_{t,dis} + P_{grid,t}^{+} + \sum_{j \ne i} P_{trade,ji,t} \\ &= P_L(t) + P_{t,ch} + P_{grid,t}^{-} + \sum_{j \ne i} P_{trade,ij,t} \end{aligned} \tag{36}$$

where $P_L(t)$, $P_{pv}(t)$, and $P_{pw}(t)$ denote the load demand, PV output, and wind output, $P_{grid,t}^{+}$ and $P_{grid,t}^{-}$ denote grid purchase and sale power, $P_{trade,ij,t}$ and $P_{trade,ji,t}$ denote the incoming and outgoing P2P trading powers of BSMG i, respectively. Since P2P transactions are matched from surplus BSMGs to deficit BSMGs, each BSMG pair is assigned a single trading direction within a scheduling interval, thereby excluding simultaneous bidirectional trading. Eq. (34) maintains capacity consistency, while Eq. (35) describes the time-coupled SoC evolution.

The prediction accuracy and goodness of fit are evaluated using the root mean square error (RMSE) and the coefficient of determination (R^2), respectively, as defined below:

$$RMSE = \sqrt{\frac{\sum_{i=1}^{N} (y_i - \hat{y}_i)^2}{N}} \tag{37}$$

$$R^2 = \frac{\sum_{i=1}^{N} (\hat{y}_i - \bar{y})^2}{\sum_{i=1}^{N} (y_i - \bar{y})^2} \tag{38}$$

where y_i denotes the actual value from the multi-dimensional dataset (including wind and PV output, load, energy storage, and trading data), $\hat{y}_i$ is the corresponding predicted value generated by the model, $\bar{y}$ is their sample mean, and N is the total number of samples.

C. Communication-Availability Model for BSMG Coordination

In the considered 5G-enabled BSMG system, communication links serve as the primary conduit for exchanging forecasting results, surplus/deficit information, trading prices, and dispatch-related coordination signals. Accordingly, communication failures are modeled at the coordination-information layer, that is, as degradation, delay, or unavailability of the information-exchange channel required for real-time P2P trading, rather than as physical interruptions of the power-transfer path. This interpretation is consistent with established communication-failure-aware microgrid studies, where collaboration information may be lost, delayed, or rendered obsolete due to communication failures or packet loss [22], [23].

To capture the operational impact of communication degradation, this study introduces a communication-availability model for each communication link I_{ij} between BSMG i and BSMG j at scheduling interval t. The model explicitly accounts for three key IoT-relevant indicators: latency $\tau_{ij,t}$, packet loss rate $\rho_{ij,t}$, and available bandwidth $B_{ij,t}$. These indicators are selected because latency, packet loss, bandwidth requirement, and link reliability are widely recognized as important

communication factors in microgrid and smart-grid applications [53], [54]. In addition, P2P energy trading relies on timely information exchange among market participants, making communication infrastructure an important enabler of real-time trading coordination [55].

Based on the quality of service (QoS) and application-specific requirements [53]–[55], a threshold-based binary communication-availability variable $a_{ij,t}$ is introduced to indicate whether the communication link can reliably support coordinated BSMG trading:

$$\begin{cases} a_{ij,t} = 1, \text{if} \tau_{ij,t} \le \tau_{\max}, \rho_{ij,t} \le \rho_{\max}, B_{ij,t} \ge B_{\min} \\ a_{ij,t} = 0, \text{otherwise} \end{cases} \tag{39}$$

where τ_{max}, ρ_{max}, and B_{min} denote the maximum tolerable latency, maximum tolerable packet loss rate, and minimum bandwidth required for reliable BSMG coordination, respectively. When $a_{ij,t} = 1$, BSMG i and BSMG j can exchange price, forecast, surplus/deficit, and trading-command information. When $a_{ij,t} = 0$, the corresponding communication link is regarded as unavailable or severely degraded for real-time coordinated trading. Here, $a_{ij,t}$ represents service-level communication availability at the scheduling layer rather than detailed packet-level network dynamics.

Accordingly, the communication thresholds in Eq. (39) are calibrated against representative 5G-enabled smart-grid requirements. Based on 3GPP TS 22.104 [56], the maximum end-to-end latency is set to τ_{max}=100 ms with reference to distributed voltage control, while the minimum available-bandwidth threshold is set to B_{min}=100 kbit/s based on the downlink data-rate requirement for distributed-energy-storage communication. The packet-loss threshold is set to $\rho_{max}=10^{-3}$, using the standardized 5G QoS Identifier (5QI) value 3 packet error rate in 3GPP TS 23.501 [57]. Its example services include medium-voltage electricity distribution and process-automation monitoring. These thresholds are adopted as representative bounds for scheduling-level BSMG information exchange rather than protection-level communication requirements.

The communication-availability matrix at time t is denoted as $A_t = [a_{ij,t}]$. Since P2P trading requires timely exchange of coordination information, A_t is embedded into the trading-capacity constraint:

$$0 \le P_{trade,ij,t} \le a_{ij,t} P_{trade,\max,ij} \tag{40}$$

where $P_{trade,ij,t}$ is the P2P trading power from BSMG i to BSMG j, and $P_{trade,max,ij}$ is the maximum allowable trading capacity between the two BSMGs. Through Eq. (40), communication availability is directly coupled with the energy-trading layer: an unavailable link forces the corresponding P2P trading power to zero, and the resulting imbalance must be compensated by local storage, the main grid, or other available BSMG links.

This formulation explicitly treats communication failures as information-exchange constraints that affect coordination feasibility, rather than as physical power-transfer interruptions. By mapping latency, packet loss, and bandwidth limitations to P2P trading feasibility, the model provides a tractable scheduling-level representation of how communication QoS affects BSMG coordination. Physical power-transfer interruptions, such as line outages or converter faults, are treated as separate fault scenarios and remain outside the scope of the present communication-failure model. This distinction ensures that the fault scenarios analyzed in this study are clearly understood as communication-constrained trading cases rather than physical infrastructure failures. The proposed binary abstraction does not explicitly represent intermediate packet-level degradation states, which remain an important direction for future communication–energy co-simulation studies.

D. Fault-Aware Transaction Cost Model

Under normal communication conditions, BSMGs can exchange real-time information with both the main grid and neighboring microgrids, enabling each unit to select economical trading partners and maintain overall supply–demand balance. In this study, the communication condition is represented by the availability matrix A_t defined in Section IV-C. When $a_{ij,t} = 1$, the communication link between BSMG i and BSMG j can support coordinated P2P trading. When $a_{ij,t} = 0$, this link is removed from the feasible trading set.

This setting represents an information-exchange constraint, the link cannot reliably exchange the price, forecast, surplus/deficit, and trading-command information required for real-time coordinated trading. It does not imply that the physical power-transfer path between the two BSMGs is disconnected. Physical power flow remains technically feasible even when the communication link is unavailable. However, without reliable coordination information, P2P trading is suspended because the participating BSMGs cannot safely agree on trading terms or dispatch schedules. This interpretation is consistent with the communication-failure-aware microgrid literature, where communication degradation is treated as an operational constraint on coordination rather than as a physical infrastructure fault [22], [23].

When certain communication links become unavailable, the affected BSMGs cannot reliably exchange real-time data on energy prices, surplus/deficit status, or trading commands. To ensure load satisfaction and operational reliability under such uncertainty, these BSMGs must adopt conservative trading strategies that prioritize transactions with the main grid or with other available BSMG links. This disruption of optimal information exchange may lead to suboptimal dispatch, reduced utilization of local renewable generation, and increased operational costs. In this context, forecasting becomes a practical resilience lever rather than a separate prediction task. When real-time coordination is degraded, accurate forecasts provide anticipatory information on local generation and demand, enabling each BSMG to make more reliable dispatch and trading decisions despite incomplete communication support.

To quantitatively evaluate the economic impacts of communication degradation, a unified cost model is developed to describe the operational behavior of the BSMG system under normal and communication-constrained conditions. The total operating cost is decomposed into three major components. The first component represents energy transactions between the BSMG cluster and the main grid. This cost reflects the external market interaction required to balance supply and demand, which typically increases when inter-BSMG coordination becomes restricted. The second component accounts for the internal energy-storage operation cost, including the efficiency losses and degradation associated with charging and

discharging processes. The third component corresponds to energy exchanges among interconnected BSMGs, which are calculated subject to the communication-constrained trading feasibility condition defined in Section IV-C. By combining these three cost components, the proposed model evaluates how forecasting quality affect fault resilience and operational decision performance under varying communication conditions.

$$C_{net} = C_{grid}(t) + C_{ES}(t) + C_{MG2MG}(t) \quad (41)$$

$$C_{grid}(t) = \sum_{t=1}^{T} (\pi_t^{buy} P_{grid}^{t,+} - \pi_t^{sell} P_{grid}^{t,-}) \quad (42)$$

$$C_{ES}(t) = \sum_{t=1}^{T} c_{bat} (P_{t,dis} / \eta + P_{t,ch}\eta) \quad (43)$$

$$C_{MG2MG}(t) = \sum_{t=1}^{T} (\pi_t^{MG,buy} P_{MG2MG}^{t,+} - \pi_t^{MG,sell} P_{MG2MG}^{t,-}) \quad (44)$$

where C_{net} is the total operating cost, $C_{grid}(t)$ is the main grid transaction cost, $C_{ES}(t)$ denotes the ES charging and discharging loss cost, $C_{MG2MG}(t)$ is the internal BSMG exchange cost, $P_{grid}^{t,+}$ and $P_{grid}^{t,-}$ are grid buy and sell volumes at prices π_t^{buy} and π_t^{sell}, $P_{MG2MG}^{t,+}$ and $P_{MG2MG}^{t,-}$ are inter-BSMG buy and sell volumes at prices $\pi_t^{MG,buy}$ and $\pi_t^{MG,sell}$, and c_{bat} is the unit cost of ES cycling losses.

When link failures occur, unavailable or delayed data may invalidate the optimal energy delivery plan, forcing a microgrid to transact with the main grid or alternative partners with higher energy transaction costs. The resulting increase in C_{grid} and C_{MG2MG} reflects the economic penalties of reduced communication reliability. Through proactive forecasting, the proposed meta-learning--based framework enables BSMGs to predefine alternative trading strategies under predicted fault conditions, thereby mitigating the additional costs and maintaining near-optimal system operation.

E. Operational Feasibility and Modeling Scope

To clarify the operational scope of the proposed model, this study adopts a scheduling-level transaction-cost formulation rather than a full AC voltage-constrained optimal power-flow (AC-OPF) formulation. This modeling choice is deliberate and aligns with established communication-failure-aware microgrid studies, which commonly focus on the operational impact of degraded information exchange and forecasting-assisted mitigation, while adopting simplified electrical representations rather than detailed feeder-level AC-OPF models.

For example, Zhou et al. [22] studied multiagent microgrid energy management under communication failures using a Bayesian deep reinforcement learning (BA-DRL) framework. Their focus is on collaborative energy-management performance under packet loss and communication uncertainty, without modeling feeder-level voltage, reactive-power, or detailed line-loss constraints. Arbab-Zavar et al. [23] investigated communication link failures in microgrids and proposed a DL-based forecasting strategy to enhance message content and support energy-storage operation during link loss. Their study evaluates the effect of communication link loss on microgrid power management through point of common coupling (PCC) power-exchange behavior, but does not formulate a full AC-OPF model. More recently, Löser et al. [58] developed a model predictive control (MPC)-based operation strategy for microgrids under communication failures and explicitly distinguished communication failure from electrical disconnection. Their formulation includes scheduling-level constraints such as power balance, unit limits, storage dynamics, and linear line-flow limits, while network losses are neglected and detailed AC voltage and reactive-power constraints are not modeled.

Motivated by these studies, the present work focuses on the scheduling-level feasibility of communication-constrained BSMG trading. The operational constraints considered in this study include:

1) Power balance constraints ensuring supply–demand equilibrium at each BSMG.

2) ES charging/discharging power limits.

3) SoC limits for battery ES systems.

4) Grid-exchange limits constraining power transactions with the main grid.

5) Communication-constrained P2P trading limits, where the trading capacity is coupled with the communication-availability variable $a_{ij,t}$ defined in Section IV-C. Specifically, when $a_{ij,t} = 0$, the corresponding trading link is excluded from the feasible trading set.

Accordingly, this study does not aim to solve a detailed feeder-level AC-OPF problem. Instead, it evaluates how communication degradation and forecasting accuracy affect feasible trading routes, transaction-cost redistribution, and the economic resilience of interconnected BSMGs. Feeder-level voltage-security analysis, reactive-power coordination, detailed line-loss modeling, explicit reserve scheduling, and robust uncertainty-constrained dispatch are recognized as important extensions that would enrich the current framework, and are therefore identified as clear directions for future work.

V. CASE STUDY

To verify the effectiveness and computational efficiency of the proposed framework, extensive simulations are conducted in Python on a computer equipped with an Intel Core i7-13700H CPU (2.40 GHz, 13th Gen) and 32 GB RAM. The simulations start with the training of the base-model ensemble and the second-level RF stacking model, then generate hourly forecasts, and evaluate dispatch costs using the proposed transaction-cost model. Performance is compared under normal communications and under link-failure scenarios with forecast-guided trade reallocation to assess adaptability and robustness. It is worth noting that the fault scenarios considered in the case studies correspond to communication-constrained trading cases, where one or more communication links are unavailable for information exchange. These scenarios should be distinguished from physical power-transfer interruptions, such as line outages or converter failures, which are not modeled here. Under communication-link unavailability, the physical power-transfer infrastructure remains intact, but trading is suspended due to the absence of reliable coordination information.

A. Data Preparation

The wind and PV generation profiles are obtained from ISO New England (https://www.iso-ne.com/search?query=dataset), while the BS load profiles are taken from the AI-for-Good "5G Base Station Power Consumption" dataset (https://aiforgood.itu.int/event/5g-energy-consumption-modelling-ai-ml-solutions-for-climate-change/). We analyze a full year of data at 1-hour resolution (8,760 points per series). Because plotting the entire year at hourly granularity results in an over-crowded figure, Fig. 5 shows the raw wind, PV, and load outputs for all five BSs over a representative one-week period (168 hours).

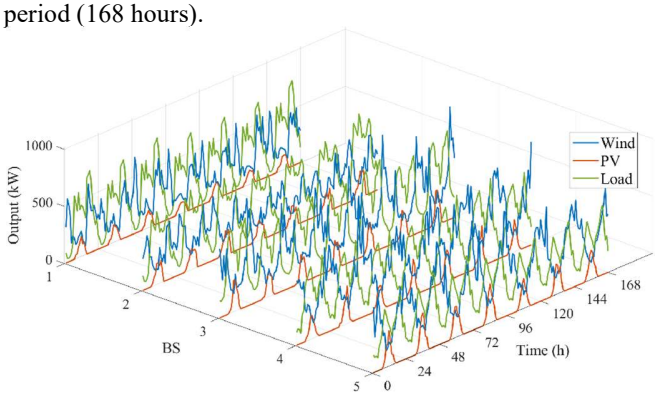


Fig. 5. Raw wind, PV and load output of BSs.

We use the Nord Pool market's grid purchase and sale prices to represent the trading prices between BSMGs (https://data.nordpoolgroup.com/auction/day-ahead/prices). In particular, when one BS buys from another within the same microgrid, it pays a rate lower than the microgrid's cost of importing electricity from the main grid, while when it sells to a peer, it receives a rate higher than the microgrid's export price back to the main grid. This pricing scheme encourages local energy exchanges before resorting to more expensive transactions with the main grid.

Historical P2P transaction data among BSMGs are not readily available in public repositories, reflecting the nascent stage of practical BSMG energy-trading deployments and the site-specific nature of such records, which depend on local market rules, private trading behavior, and communication availability. Consequently, synthetic trading records are generated to evaluate the proposed framework under controlled and reproducible conditions.

This approach is consistent with established practice in microgrid energy-management studies under communication failures, where simulation-based trading environments are commonly employed when field-recorded transaction data are unavailable. For example, Zhou et al. [22] modeled microgrid energy trading through a bidding-based platform, where suppliers submit power supply capacities and bidding prices, consumers submit demand, and the clearing price is determined by the intersection of total supply and demand. In their simulation, PV power is generated from a reference source with Gaussian prediction errors, and bidding prices are discretized into predefined price levels.

The synthetic trading records in this study are generated through the following procedure:

Step 1 – Economic dispatch: An hourly economic dispatch is conducted for each BSMG based on Nord Pool price signals alongside load and renewable generation profiles. This yields a net import and export schedule relative to the main grid, where positive values indicate net purchases and negative values indicate net sales.

Step 2 – P2P trade operationalization: The net import and export positions are operationalized as P2P trades using an hourly balancing mechanism. For each hour, the aggregate surplus across the BSMG cluster is matched against the aggregate deficit, and the available surplus is apportioned to deficit microgrids according to their relative shortfalls. Any residual imbalance that cannot be resolved internally is settled through exchanges with the main grid.

Step 3 – Noise injection for realistic variability: To reflect the inherent uncertainty in real-world market operations, zero-mean Gaussian noise with time-dependent standard deviation is applied to each internal trade—σ=3.0% during off-peak hours and σ=7.0% during the evening peak period (18:00–22:00). Noise values are truncated to ±20% to prevent physically implausible outliers, and microgrid-specific physical trading constraints are enforced.

This methodology produces a P2P trading history that captures both the economic signals of the main market and plausible internal exchange behaviors, providing a physically consistent and operationally meaningful basis for evaluating the proposed coordination framework.

B. Results of data analysis

The comprehensive dataset scores are obtained by applying the hierarchical evaluation framework defined in Eqs. (13)-(26). Table II presents five evaluation metrics for each of the four dataset groups. In the all days group, the smallest ADF indicates strongest stationarity, the highest H shows greatest persistence, the smallest SS reflects the most intense nonperiodic fluctuations, the highest ApEn denotes greatest complexity, and the moderate TRVR indicates a balanced noise component. These results demonstrate that no single metric or even a subset can fully characterize a series or guide optimal model selection due to their conflicting outcomes. Thus, an integrated decision-making mechanism is needed to balance multiple criteria.

TABLE II
DATA ANALYSIS RESULTS OF DIFFERENT DATASETS

Group	Dataset	ADF	SS	ApEn	H	TRVR
1st: Full-year	All days	6.7E-05	0.555	0.930	0.572	0.0001
	Weekdays	5.9E-04	0.562	0.921	0.569	0.0010
	Weekends	0.0168	0.556	0.886	0.553	0.0103
2nd: Full-year seasons	Spring	6.1E-06	0.568	0.848	0.441	0.00586
	Summer	7.2E-06	0.573	0.857	0.460	0.00628
	Autumn	4.5E-06	0.570	0.861	0.451	0.00594
	Winter	4.7E-05	0.561	0.856	0.468	0.00504
3rd: Weekday seasons	Spring	2.8E-05	0.572	0.827	0.463	0.00738
	Summer	1.3E-04	0.577	0.846	0.460	0.00570
	Autumn	9.2E-06	0.582	0.845	0.454	0.00633
	Winter	6.2E-04	0.565	0.834	0.456	0.00565
4th: Weekend seasons	Spring	4.8E-14	0.552	0.774	0.470	0.00442
	Summer	6.0E-15	0.613	0.769	0.478	0.00700
	Autumn	1.3E-14	0.587	0.777	0.465	0.00460
	Winter	2.1E-07	0.562	0.782	0.492	0.00685

C. Scoring results of the dataset

Since forecasting models exhibit different strengths

depending on data stability and statistical complexity, the datasets are first scored and categorized into four tiers to guide model selection (Table III). The tiered structure is intentionally designed to include a small number of representative models from each modelling type, rather than an arbitrarily large set. This design balances predictive diversity, computational tractability, and ensemble interpretability.

Tier 1 (score ⩾ 0.98) employs three statistical models (ARIMA, SARIMA, Prophet), as these methods share similar linear structures and adding more variants would provide limited additional benefit.

Tier 2 (0.96-0.98) augments Tier 1 with three ML models (XGBoost, LightGBM, CatBoost), each representing a distinct gradient-boosting mechanism and offering complementary nonlinear modelling capabilities.

Tier 3 (0.94-0.96) further extends the ensemble with two DL architectures (LSTM and Transformer), selected as the dominant representatives of memory-based and attention-based sequence modelling.

Tier 4 (score < 0.94) introduces two RL agents (DQN and PPO), capturing value-based and policy-based decision types without imposing excessive computational overhead.

Overall, limiting each tier to 1-3 well-established models avoid redundancy, prevents inflated training cost, and preserves the interpretability of the multi-layer ensemble, while still ensuring adequate methodological diversity across modelling families.

TABLE III
MODEL COMPLEXITY TIERS

Tier	Score
Tier 1 (Statistical model)	Score ≥ 0.98
Tier 2 (Statistical+ML)	0.96 ≤Score < 0.98
Tier 3 (Statistical+ML+DL)	0.94 ≤Score < 0.96
Tier 4 (Statistical+ML+DL+RL)	Score < 0.94

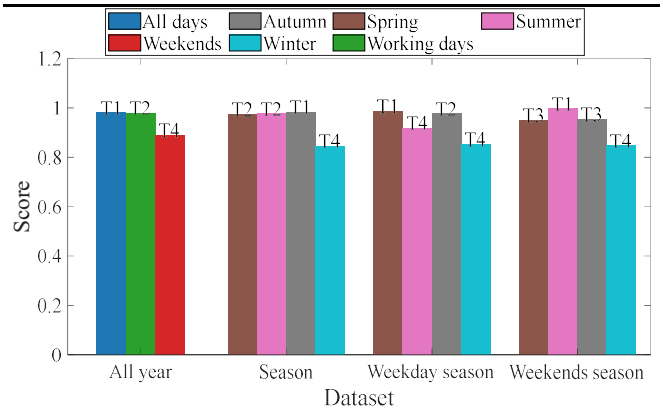


Fig. 6. Scores of datasets in different groups.

Fig. 6 shows scores for 15 datasets across four grouping schemes, with each bar labeled by its model complexity tier. In group 1, the all days dataset scores highest (0.981, T1), reflecting maximum stability. The weekdays dataset follows at 0.979 (T2), making it suitable for additional ML methods. The weekends dataset scores lowest (0.890, T4) and requires to combine the statistical, ML, DL, and RL approaches. In group 2, the autumn dataset is highly stable (0.984, T1), spring and summer datasets favor statistical + ML methods (0.975, T2), and winter dataset is most volatile (0.845, T4), requiring the most complex solution. In group 3, spring dataset (0.987, T1) and autumn dataset (0.977, T2) are stable, while summer dataset (0.920, T4) and winter dataset (0.852, T4) require DL plus RL methods. In group 4, summer dataset is extremely stable (0.997, T1), spring and autumn datasets show moderate fluctuation (0.949–0.955, T3), and winter dataset is least stable (0.846, T4). Overall, high scores (T1/T2) allow simple statistical or statistical + ML models, while low scores (T3/T4) call for DL or RL to enhance prediction performance.

To assess the robustness of the four-tier model assignment across datasets with different stability characteristics, a threshold sensitivity analysis is conducted for all four dataset groups. The baseline boundaries of 0.98, 0.96, and 0.94 are perturbed by ±0.01 while maintaining the original four-tier structure:

1) Lower-threshold setting: Boundaries shifted downward to 0.97, 0.95, and 0.93.

2) Upper-threshold setting: Boundaries shifted upward to 0.99, 0.97, and 0.95.

As summarized in Table IV, tier changes occur mainly for datasets close to the decision boundaries, whereas highly stable or highly volatile datasets generally retain their assignments. In Group 1, the lower setting reclassifies the weekday dataset from T2 to T1, while the upper setting shifts the all-days dataset from T1 to T2. Similar adjacent-tier changes are observed in groups 2–4: spring/summer/autumn subsets in group 2, spring/autumn in group 3, and spring/autumn in group 4 are affected as the thresholds vary.

Compared with the lower setting, the baseline thresholds reduce the average RMSE from 0.125 to 0.113 and increase R^2 from 0.770 to 0.823, while runtime increases from 12.8 to 14.6 min. Increasing the thresholds further raises the runtime to 18.1 min, but provides only limited additional improvement. Groups 2–4 show the same general tendency: the baseline setting improves forecasting accuracy relative to the lower setting, whereas higher thresholds further increase computational cost and provide smaller or dataset-dependent additional gains.

Overall, the baseline threshold configuration (0.98, 0.96, 0.94) provides the most practical balance between forecasting accuracy and computational cost. It preserves useful model diversity for boundary datasets while avoiding unnecessary complexity for stable datasets. The sensitivity analysis confirms that the tiered selection mechanism is robust to threshold variations and that the baseline thresholds are empirically justified.

TABLE IV
THRESHOLD SENSITIVITY ANALYSIS OF FOUR-TIER ASSIGNMENT

Dataset	Metric	Decreased threshold	Baseline thresholds	Increased threshold
Group 1	Tier assignment	T1/T1/T4	T1/T2/T4	T2/T2/T4
	Avg. RMSE	0.125	0.113	0.112
	Avg. R^2	0.770	0.823	0.828
	Avg. runtime	12.8 min	14.6 min	18.1 min
Group 2	Tier assignment	T1/T1/T1/T4	T2/T2/T1/T4	T2/T2/T2/T4
	Avg. RMSE	0.116	0.101	0.095
	Avg. R^2	0.779	0.797	0.802
	Avg. runtime	5.2 min	6.1 min	6.6 min
Group 3	Tier assignment	T1/T4/T1/T4	T1/T4/T2/T4	T2/T4/T2/T4
	Avg. RMSE	0.110	0.099	0.095
	Avg. R^2	0.750	0.809	0.814

	Avg. runtime	4.5 min	4.9 min	5.3 min
	Tier assignment	T3/T1/T2/T4	T3/T1/T3/T4	T4/T1/T3/T4
Group 4	Avg. RMSE	0.148	0.137	0.116
	Avg. R^2	0.736	0.785	0.790
	Avg. runtime	2.6 min	2.9 min	3.4 min

D. Prediction results of BSMG actions

A hierarchical data splitting strategy enhances generalization and robustness, ensures proper hyperparameter tuning, and provides unbiased evaluation across temporal patterns. The data are first treated as a single annual category, then divided into spring, summer, fall and winter, next split into weekdays and weekends, and finally subdivided into weekday and weekend subsets within each season. Each subset is split into 80% training, 10% validation, and 10% testing sets, as shown in Fig. 7.

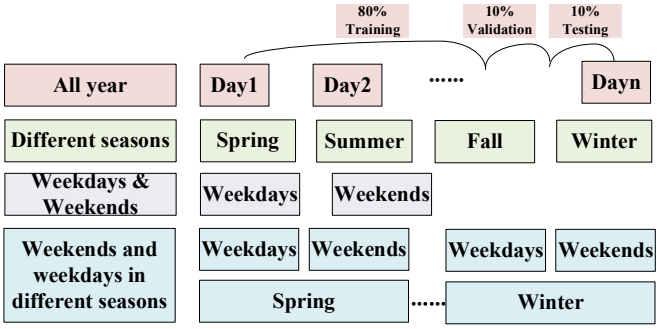
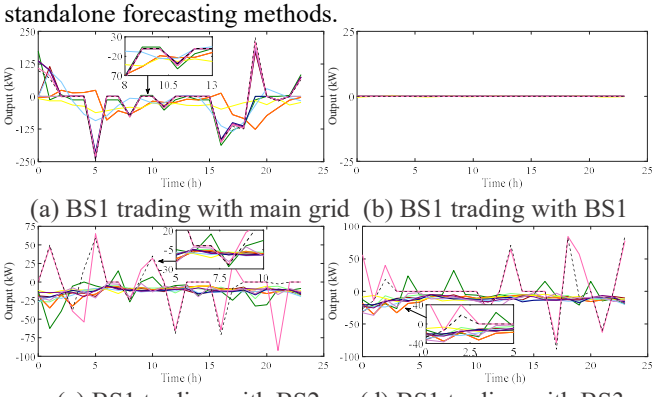


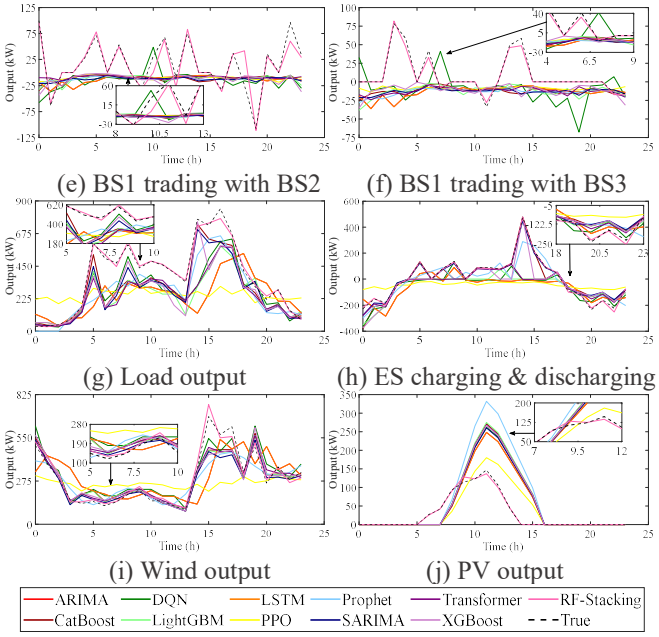
Fig. 7. Partitioning of the dataset.

Fig. 8 illustrates one representative day of forecasting results for BS1 across all data dimensions in the all-days dataset of group1. The figure provides an overall visual comparison of the temporal trends produced by different forecasting methods. RF-Stacking generally tracks the true trajectories more closely than the individual base models, particularly around sharp fluctuations. However, because the magnitudes of deviations are difficult to discern visually, especially when multiple methods are plotted simultaneously, the figure alone cannot fully reveal the performance gap among models. Therefore, the quantitative accuracy metrics reported in Table V complement Fig. 8 by providing a clearer and objective comparison. These metrics confirm that RF-Stacking consistently achieves lower prediction errors than any single model across all data types. Together, Fig. 8 and Table V demonstrate that the RF-Stacking method offers more stable and accurate forecasts than standalone forecasting methods.



(a) BS1 trading with main grid (b) BS1 trading with BS1

(c) BS1 trading with BS2 (d) BS1 trading with BS3



(e) BS1 trading with BS2 (f) BS1 trading with BS3

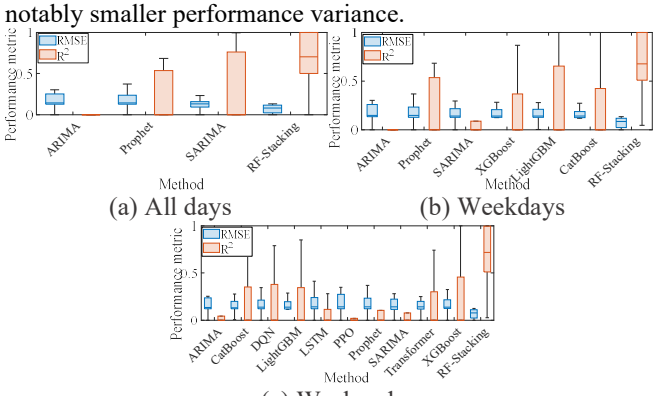
(g) Load output (h) ES charging & discharging

(i) Wind output (j) PV output

Fig. 8. Prediction results for BS1 over the all-year period.

E. Prediction accuracy

Fig. 9 displays the group 1's performance in three panels. Each panel uses a tailored pool of methods based on precomputed stability scores: the all-days dataset only tests statistical models plus RF-Stacking, the weekdays dataset adds ML approaches, and the weekends dataset further includes DL and RL methods. As a result, errors remain tight and low in broader datasets in Fig. 9(a), grow moderately in Fig. 9 (b), and swing widely in Fig. 9(c) when using single methods alone. Table V summarizes the mean RMSE and R^2 values across group 1. Even compared with the highest R^2 achieved by any single model in each dataset, RF-Stacking still delivers 3%–20% higher R^2 and 14%–53% lower RMSE on average, with notably smaller performance variance.



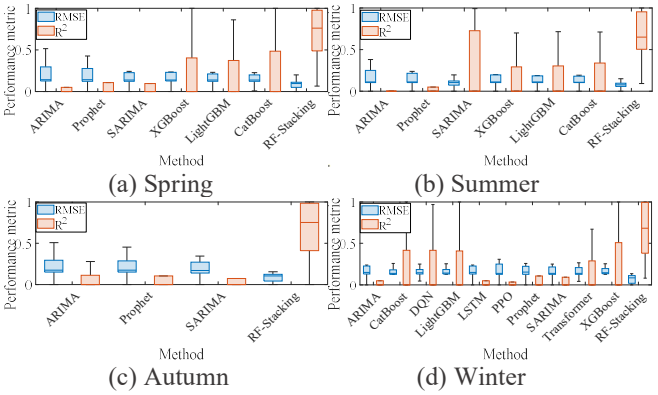
(a) All days (b) Weekdays

(c) Weekends

Fig. 9. BS1 evaluation metrics comparison (Group1).

Fig. 10 compares the four seasonal datasets within group 2. Applying statistical and ML methods to the spring and summer datasets (Fig. 10(a–b)) results in lower errors and higher R^2, but with increased variance in performance. Fig. 10(c) autumn of Tier 1, simple models deliver tight RMSE and lower R^2 while RF-Stacking outperforms with minimal variance. In Fig. 10(d) of Tier 4, standalone models swing widely, yet RF-Stacking still achieves the lowest RMSE and highest R^2 with the

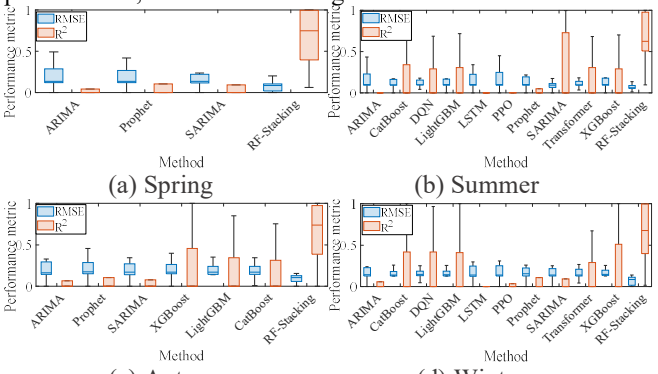
narrowest boxes.



(a) Spring (b) Summer (c) Autumn (d) Winter

Fig. 10. BS1 evaluation metrics comparison (Group2).

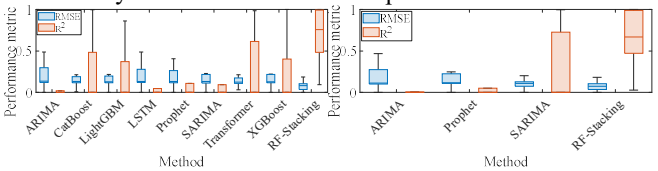
Fig. 11 compares the seasonal weekday datasets from group 3. Fig. 11(a) shows the spring dataset, corresponding to a Tier 1 scenario, where statistical models yield low, consistent errors but only modest R^2, while RF-Stacking achieves superior accuracy with minimal variance. Fig. 11(b) presents the summer dataset, a Tier 4 case involving all model types. Here, standalone ML, DL, and RL methods exhibit large fluctuations in error, yet the ensemble still achieves the lowest RMSE and highest R^2. Fig. 11(c) illustrates the autumn dataset, a Tier 2 setting, where adding ML to statistical models slightly reduces RMSE and improves R^2, albeit with increased variability. RF-Stacking again provides the best balance of accuracy and stability. Fig. 11(d) shows the winter dataset, representing another Tier 4 case, where individual methods vary widely in performance, while RF-Stacking remains the most accurate.

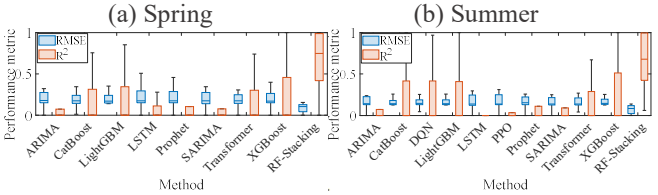


(a) Spring (b) Summer (c) Autumn (d) Winter

Fig. 11. BS1 evaluation metrics comparison (Group3).

Fig. 12 illustrates the seasonal weekend datasets from group 4. Fig. 12(b) presents the summer dataset, a Tier 1 case, where statistical models yield tight RMSE but modest R^2. Fig. 12(a) and Fig. 12(c) correspond to the spring and autumn datasets, both Tier 3 splits, where adding DL to statistical and ML models reduces RMSE and enhances R^2, though standalone methods show greater variability. Fig. 12(d) shows the winter dataset, a volatile Tier 4 case, where the full model set causes large swings in RMSE and R^2. Across all subsets, RF-Stacking consistently delivers the most stable performance.





(a) Spring (b) Summer (c) Autumn (d) Winter

Fig. 12. BS1 evaluation metrics comparison (Group4).

The performance differences observed across Figs. 9-12 are not merely numerical, but can be explained by the interaction between dataset complexity and model characteristics. In lower-tier or broader datasets, the data distributions are more regular and stationary, allowing statistical models to achieve relatively low and stable RMSE. However, their limited representational capacity often leads to only modest R^2, indicating that they capture the dominant trend but fail to explain finer temporal variability. As the datasets become more heterogeneous, such as in weekday, weekend splits or Tier 3-4 seasonal subsets, standalone ML, DL, and RL models gain flexibility but also become more sensitive to noise, sample sparsity, and distribution shifts, which explains their larger performance variance. In contrast, RF-Stacking consistently performs better because it integrates predictors with different inductive biases, reducing over-reliance on any single model and achieving a more robust balance between accuracy and stability across diverse scenarios.

TABLE V
MEAN RMSE AND R^2 VALUES FOR DIFFERENT METHODS ON GROUP 1

Dataset	Method	RMSE	R^2
All days	ARIMA	0.20	0.19
	Prophet	0.21	0.11
	SARIMA	0.19	0.14
	RF-Stacking	0.09	0.88
Weekdays	ARIMA	0.23	0.26
	Prophet	0.24	0.02
	SARIMA	0.21	0.15
	XGBoost	0.16	0.20
	LightGBM	0.15	0.41
	CatBoost	0.20	0.18
	RF-Stacking	0.12	0.81
Weekends	ARIMA	0.19	0.07
	CatBoost	0.20	0.18
	DQN	0.21	0.15
	LightGBM	0.23	0.17
	LSTM	0.24	0.12
	PPO	0.26	0.05
	Prophet	0.23	0.13
	SARIMA	0.22	0.11
	Transformer	0.21	0.14
	XGBoost	0.22	0.33
	RF-Stacking	0.13	0.78

F. Operational cost discussion

This study evaluates the transaction costs of the BSMG system under normal operation and under two-BSMG and three-BSMG communication-unavailability scenarios. In the normal operating condition, BSMGs can exchange real-time information with neighboring BSMGs and the main grid, enabling coordinated energy trading and cost-effective power balancing. For each BSMG pair, the communication state is determined from the corresponding latency, packet-loss rate,

and available bandwidth according to Eq. (39). If any communication variable violates its prescribed threshold, $a_{ij,t}$=0, and the corresponding P2P trading link is excluded from the feasible trading set through Eq. (40).

For instance, as illustrated in Fig. 13, BS1 normally trades directly with BS3 to minimize transaction costs. When the BS1–BS3 communication state is classified as unavailable by Eq. (39), the corresponding P2P trading link is removed, and BS1 must reallocate its power exchange through other available BSMGs or the main grid, leading to higher transaction expenses. In two-BSMG communication-unavailability scenarios, the affected BSMGs cannot reliably exchange forecasts, surplus/deficit information, or trading commands for coordinated P2P trading. In three-BSMG communication-unavailability scenarios, the coordination capability is further reduced, and the affected BSMGs rely more heavily on alternative BSMG partners or the main grid for power balancing.

To assess the effect of forecasting, two operational modes are compared. In the forecast-enabled case, pre-scheduled trading plans use predicted generation and demand information to support proactive transaction reallocation under potential communication unavailability. In the non-forecast case, energy is redistributed reactively through random-node or nearest-neighbor selection, which may lead to suboptimal cost performance. Figs. 14–17 present the comparative results for these scenarios, showing that communication unavailability increases transaction costs, while forecasting-assisted scheduling mitigates the cost increase and enhances the economic resilience of interconnected BSMGs.

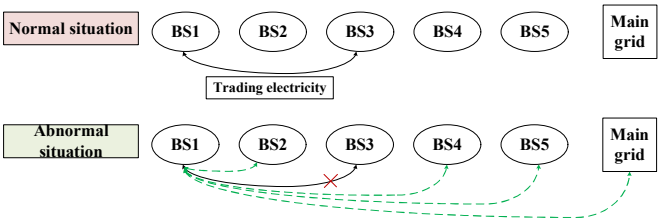
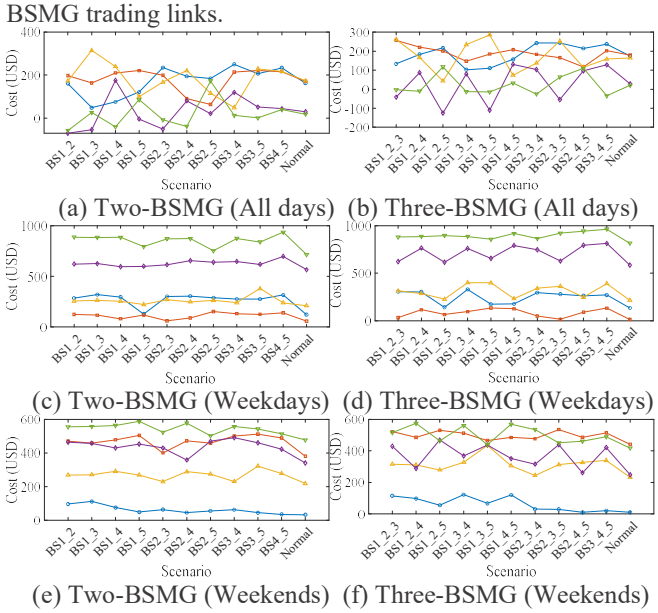


Fig. 13. Illustration of normal and communication-unavailable BSMG trading links.



(a) Two-BSMG (All days) (b) Three-BSMG (All days)

(c) Two-BSMG (Weekdays) (d) Three-BSMG (Weekdays)

(e) Two-BSMG (Weekends) (f) Three-BSMG (Weekends)

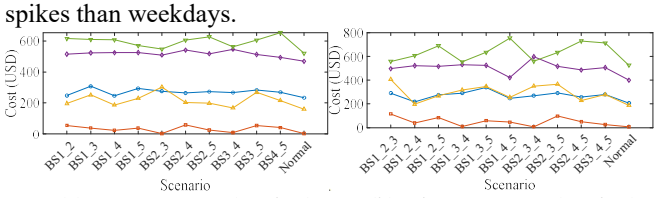


Fig. 14. Transaction costs under two-BSMG and three-BSMG communication-supported trading-link unavailability scenarios (Group 1). Two-BSMG scenarios refer to the unavailability of the communication-supported trading link between two BSMGs, such as BS1_2, while three-BSMG scenarios refer to the unavailability of communication-supported trading links among three BSMGs, such as BS1_2_3.

Fig. 14 summarizes the transaction costs of BSMG1–BSMG5 under different communication-link unavailability scenarios across all days, weekdays, and weekends. Labels such as BS1_2 and BS1_2_3 specify the BSMGs associated with the unavailable communication-supported trading links. For example, BS1_2 denotes the case in which the communication state of the BS1–BS2 link is classified as unavailable by Eq. (39), i.e., $a_{12,t}$=0, due to violation of at least one communication-quality threshold. BS1_2_3 denotes the case in which the communication states among BS1, BS2, and BS3 are classified as unavailable by Eq. (39), causing the corresponding pairwise P2P trading links to be removed through Eq. (40). "Normal" represents the baseline case with full communication availability and forecasting support. Compared with the normal case, pairwise communication-link unavailability, such as BS1_2, requires part of the trading demand to be reallocated to other available BSMGs or the main grid, shifting the cost burden among BSMGs. Group-level communication-link unavailability, such as BS1_2_3, further reduces trading flexibility and generally leads to higher transaction costs. Overall, costs are highest and most volatile on weekends, moderate on weekdays, and lowest in the all-days case.

Table VI provides a detailed breakdown of weekend transaction costs under different group-level communication-link unavailability scenarios. The normal case with forecasting achieves the lowest total cost of 1349.98 USD, while all group-level unavailability scenarios exceed 1500 USD. The highest cost occurs in the BS1_2_3 scenario, where the communication-supported trading links among BS1, BS2, and BS3 are unavailable, reaching 1898.46 USD. Compared with this worst case, the normal case reduces the total cost by approximately 29%. At the individual level, BSMG1 increases from 9.90 USD in the normal case to 115.18 USD under BS1_2_3, showing that communication-link unavailability can substantially redistribute the cost burden among BSMGs.

Figs. 15–17 show seasonal transaction costs for groups 2–4, respectively. Summer faults generally lead to the highest cost spikes, though a notable springtime peak appears during the weekend season. The other seasons exhibit moderate fluctuations. Group 3 exhibits greater seasonal fluctuations than group 2. In group 4, weekend faults show more pronounced spikes than weekdays.



(a) Two-BSMG (Spring) (b) Three-BSMG (Spring)

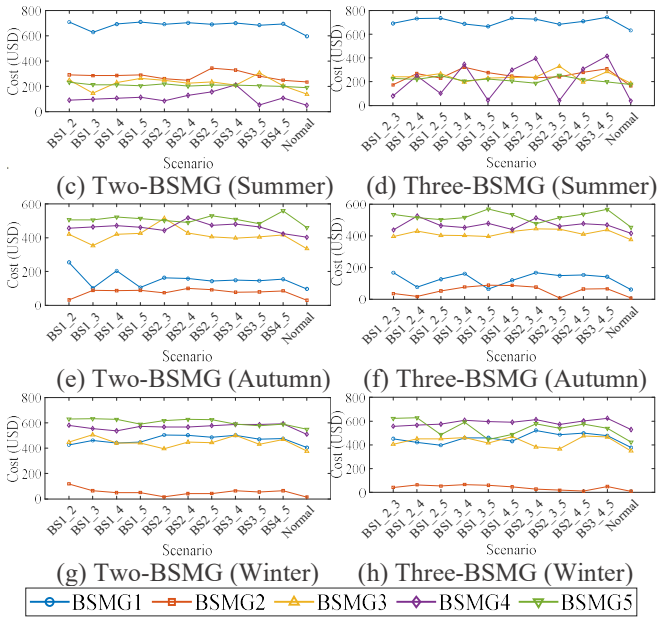


Fig. 15. Transaction costs under two-BSMG and three-BSMG communication-supported trading-link unavailability scenarios (Group2).

Communication link failures significantly increase operational costs. Compared to the normal forecasted condition, two-station faults raise costs by around 15%, while three-station faults may increase costs by up to 40%. These results confirm that accurate forecasting plays a vital role in reducing economic losses during communication disruptions.

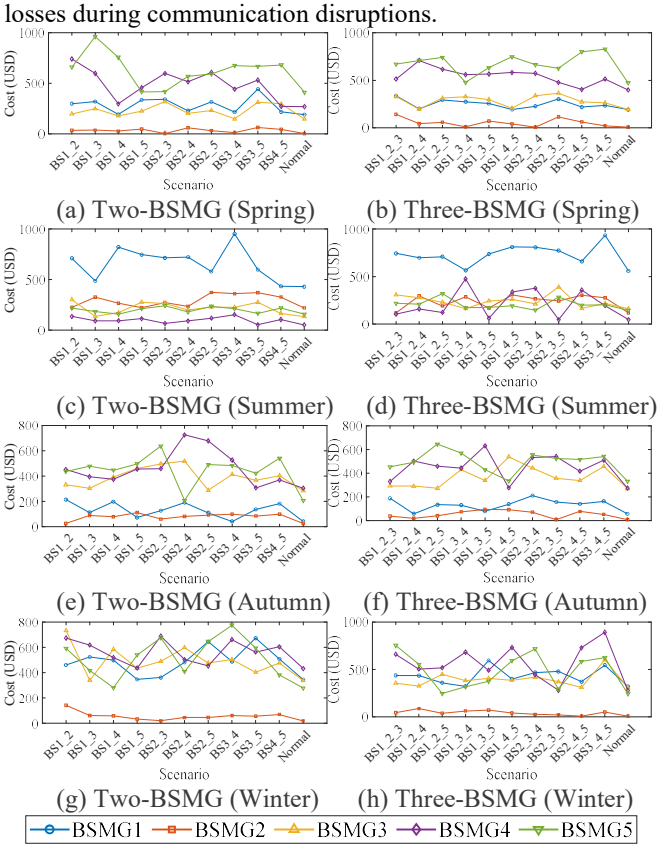


Fig. 16. Transaction costs under two-BSMG and three-BSMG communication-supported trading-link unavailability scenarios (Group3).

TABLE VI
TRANSACTION COSTS UNDER 3-LINK UNAVAILABILITY ON WEEKENDS (GROUP 1)

Scenario	BSMG1 (USD)	BSMG2 (USD)	BSMG3 (USD)	BSMG4 (USD)	BSMG5 (USD)	SUM (USD)
BS1_2_3	115.18	521.45	316.15	429.19	516.49	1898.46
BS1_2_4	97.19	485.48	310.69	289.08	574.98	1757.43
BS1_2_5	55.30	529.84	279.67	468.79	462.91	1796.51
BS1_3_4	122.29	512.39	327.68	368.17	560.02	1890.56
BS1_3_5	66.76	465.10	435.55	436.44	439.16	1843.01
BS1_4_5	120.39	484.99	305.16	350.93	568.44	1829.91
BS2_3_4	31.44	476.96	244.93	315.83	534.88	1604.04
BS2_3_5	29.53	535.13	312.51	438.47	450.81	1766.45
BS2_4_5	10.43	486.23	326.43	261.41	461.07	1545.57
BS3_4_5	20.57	514.69	339.29	421.71	489.02	1785.28
Normal	9.90	441.85	232.69	248.34	417.20	1349.98

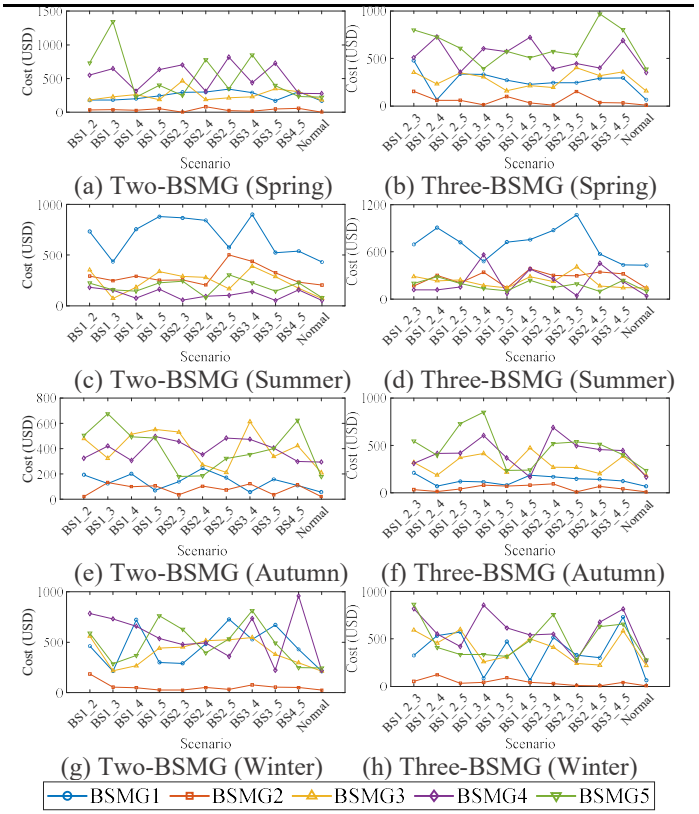


Fig. 17. Transaction costs under two-BSMG and three-BSMG communication-supported trading-link unavailability scenarios (Group4).

G. Ablation Study on Model Selection Strategy

1) Effect of indicator subset size (indicator ablation)

In these comparative simulations, the impact of metric selection on both dataset scoring and forecast accuracy is assessed. Composite GRA scores are calculated twice, first using all five indicators, then using only three key metrics (ADF p-value, seasonal strength, and approximate entropy).

Fig. 18 shows the GRA scores for all and three indicators. Each bar represents the GRA composite score for a different day type (all days, weekdays, weekends), with the left cluster based on all five indicators and the right cluster on the reduced set of three. Omitting two indicators reshapes the score hierarchy: all days no longer achieve the highest rating, and

score gaps among day types decrease, demonstrating that the reduced metric set alters dataset prioritization. Notably, using the full five indicator evaluation the weekday subset was assigned to model configuration Tier 2 (traditional models plus an ML component), whereas using only three indicators it falls into Tier 1 (traditional models only). This shift implies that the reduced metric set classifies the data as more stable, hence a simpler baseline model is selected.

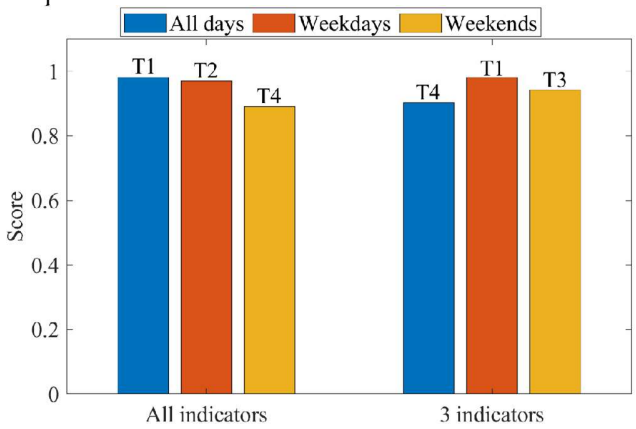


Fig. 18. Improved GRA scores for all and three indicators (Group1).

Fig. 19 presents evaluation metrics for the two indicator sets on weekdays and Table VII provides the corresponding median RMSE and R^2 values. With only three indicators, the median RMSE increases from 0.27 to 0.32 (approximately an 18.5% increase), while the median R^2 drops from 0.71 to 0.59 (about a 16.9% decrease), confirming a notable decline in forecast accuracy. This suggests that reducing the indicator set undermines model performance, and using all five evaluation indicators leads to more reliable and robust forecasting outcomes. The performance gap also highlights that the simplified model (Tier 1) selected with reduced indicators is less capable of capturing true dataset stability.

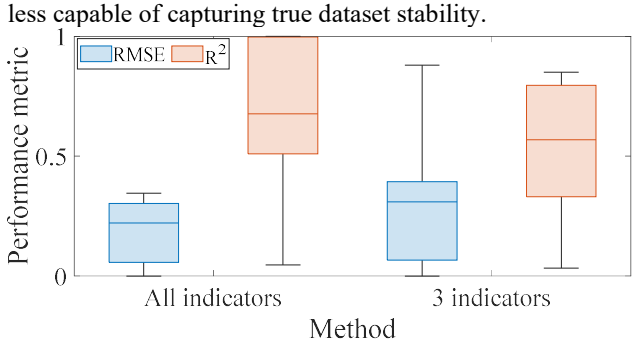


Fig. 19. Evaluation metrics for all and three indicators on weekdays (Group1).

TABLE VII
MEDIAN EVALUATION METRICS FOR DIFFERENT INDICATOR SET ON WEEKDAYS (GROUP 1)

Indicator set	RMSE	R^2
All indicators	0.27	0.71
3 indicators	0.32	0.59

2) Effect of different scoring mechanisms (scoring ablation)

Fig. 20 compares composite scores from the original GRA and the improved GRA in group 1. Using the traditional GRA the weekday dataset is placed in Tier 1, matching the outcome of the three indicators case. This leads to the simplest model choice and a drop in both forecast accuracy and goodness-of-fit. By contrast, the improved GRA ranks weekdays in Tier 2, preserving a higher model complexity that sustains accuracy. For the all days dataset, the original GRA conservatively assigns it to Tier 2, whereas the improved GRA recognizes its relative stability and places it in Tier 1, enabling more efficient use of resources. These results show that the benefit of the improved GRA is not merely a change in weighting formula, but a more balanced integration of expert preference, indicator variability, and inter-indicator correlation, which leads to more appropriate tier assignments and a better trade-off between forecasting accuracy and model complexity.

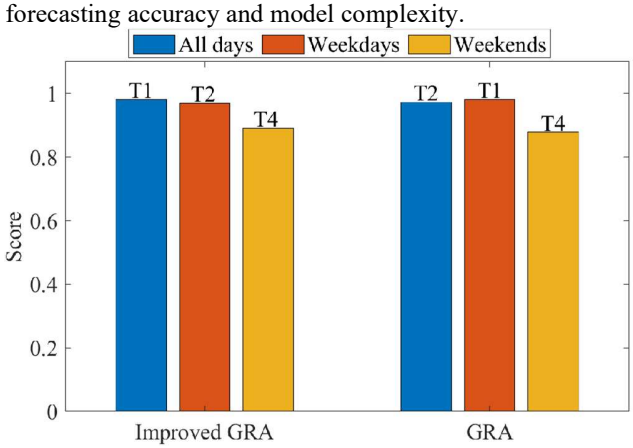


Fig. 20. Score from GRA and improved GRA on weekdays (Group 1).

3) Effect of DQN and PPO inclusion (RL-component ablation)

To quantify the contribution of the RL-based predictors, an ablation study is conducted on the group 1 weekend dataset, which is classified as Tier 4 under the proposed model-selection strategy. As shown in Table VIII, the full configuration reduces RMSE by 9.1% (from 0.143 to 0.130) and increases R^2 from 0.731 to 0.780 compared with the configuration without RL predictors, at the expense of a 3.1 min increase in computation time. The intermediate results obtained by including DQN or PPO individually indicate that both RL-based predictors contribute complementary information to the ensemble. Although they increase computational cost, similar accuracy–complexity trade-offs have been reported in recent PPO- and DQN-based forecasting studies [39], [59]. Accordingly, the RL components are selectively applied only to T4 datasets, where their additional predictive diversity produces measurable accuracy gains.

TABLE VIII
ABLATION RESULTS OF DQN AND PPO FOR THE GROUP 1 WEEKEND DATASET

Configuration	RMSE	R^2	Computation time
Without DQN and PPO	0.143	0.731	12.8 min
With DQN without PPO	0.136	0.752	14.1 min
With PPO without DQN	0.139	0.743	14.5 min
With DQN and PPO	0.130	0.780	15.9 min

H. Sensitivity Analysis

To assess whether the cost-related conclusions are contingent upon a specific synthetic trading-data configuration, we conduct a sensitivity analysis by systematically varying the

noise level applied during the P2P trading data generation process. The baseline setting introduces zero-mean Gaussian perturbations with standard deviations of σ=3.0% during off-peak hours and σ=7.0% during the evening peak period, reflecting the typically higher demand and generation variability observed during peak times. Two additional noise settings are examined: a low-noise setting using 0.5× the baseline standard deviation, and a high-noise setting using 1.5× the baseline standard deviation. For all settings, the noise values are truncated to ±20% to prevent physically implausible outliers, and the same trading feasibility constraints are enforced. Table IX summarizes the transaction costs under the three noise settings across different communication-availability scenarios. The results reveal two key findings:

First, the absolute cost values vary with noise intensity, as expected due to the increased variability in the trading records. Under the high-noise setting, transaction costs are generally higher across all scenarios compared to the baseline and low-noise settings.

Second, and more importantly, the relative cost patterns remain consistent across all three noise settings. Under all configurations, the normal communication case consistently yields the lowest transaction costs, while scenarios with two and three unavailable BSMG communication links lead to progressively higher costs. Specifically:

1) Two-BSMG communication unavailability results in cost increases ranging from 12.0% to 15.2% across the three noise settings.

2) Three-BSMG communication unavailability results in cost increases ranging from 28.2% to 34.0%.

These findings confirm that the main comparative conclusions are not artifacts of a single synthetic trading-data setting. Instead, communication unavailability consistently increases transaction costs due to reduced feasible P2P trading coordination and increased reliance on alternative BSMG trading routes or the main grid. The consistency of these relative trends across different noise levels substantiates the robustness of the proposed framework's comparative performance.

TABLE IX
SENSITIVITY ANALYSIS OF AVERAGE WEEKEND TRANSACTION COSTS UNDER DIFFERENT NOISE LEVELS (GROUP 1)

Metric	Low noise	Baseline noise	High noise
Off-peak σ	1.5%	3.0%	4.5%
Peak σ	3.5%	7.0%	10.5%
Normal case cost (USD)	1338.42	1349.98	1364.27
Two-BSMG unavailability cost (USD)	1498.36	1532.85	1571.94
Three-BSMG unavailability cost (USD)	1715.63	1771.72	1828.49
Cost increase range	12.0-28.2%	13.5-31.2%	15.2-34.0%

I. Computational Complexity and Scalability

The computational tractability of the proposed meta-learning framework is analyzed with respect to dataset size, model number, and scenario scale. The workflow consists of three stages: dataset stability assessment, first-level base model forecasting, and second-level meta-learner integration.

1) Dataset evaluation.

In the dataset evaluation stage, five stability indicators are calculated for each dataset. The computational complexity of this step is $o(\gamma_1 \cdot \gamma_2)$, where γ_1 denotes the number of time-series samples and γ_2 the number of indicators. The subsequent multi-criteria decision-making process (GRA, EWM, CRITIC, and TF-AHP) mainly involves normalization and inter-indicator weighting, yielding an overall complexity of $o(\gamma_2^2)$ per dataset.

2) First-level and baseline model.

In the first-level ensemble, statistical models (e.g., ARIMA, SARIMA) scale approximately linearly with the number of samples, i.e., $o(\gamma_1)$. ML models such as XGBoost, LightGBM, and CatBoost exhibit a computational complexity of $o(\gamma_1 \log \gamma_1)$. DL architectures, including LSTM and transformer networks, scale as $o(\gamma_1 \gamma_3^2)$, where γ_3 denotes the hidden-layer dimension. RL agents (e.g., DQN, PPO) depend on the iteration count γ_4 and the parameter size γ_5, resulting in a total complexity of $o(\gamma_4 \gamma_5)$. Among these first-level models, the DL architectures constitute the computational baseline, as they incur the highest asymptotic complexity and represent the strongest single-model forecasting capability.

3) Second-level stacking model.

At the second level, the RF stacking model integrates γ_6 base models from the first ensemble layer, with a training complexity of $o(\gamma_6 \cdot \gamma_1 \log \gamma_1)$ and inference complexity of $o(\gamma_6 \cdot \log \gamma_1)$.

4) Overall scalability.

To evaluate the practical deployability of the proposed forecasting framework, we analyze its runtime performance and scalability across dataset partitions, by seasons, weekdays, and weekends, as illustrated in Fig. 7. The runtime is measured for the complete workflow, encompassing dataset stability assessment, first-level base-model training, RF meta-learner training, and final prediction generation.

- Runtime performance across dataset scales

The full-year case, comprising 8,760 hourly samples, represents the upper bound of the computational demand. The complete workflow requires several tens of minutes on a standard computing platform. At the other extreme, the smallest seasonal weekend subset, comprising approximately 626 hourly samples, completes the same workflow within a few minutes, demonstrating the framework's efficiency for smaller-scale applications.

- Runtime breakdown and scalability characteristics

The training stage constitutes the dominant share of the total runtime, as the selected first-level base models must be trained before the RF meta-learner can be constructed. Within this stage, DL and RL models require substantially more runtime than statistical and ML models due to their iterative parameter updates and optimization procedures. This is an inherent characteristic of stacked ensemble learning, where the diversity and complementarity of the base models, spanning multiple modeling paradigms, are essential for performance.

In contrast, inference is computationally efficient. After training, the ensemble only needs to generate first-level predictions, which are forward passes through the trained base

models, and fuse them through the trained RF meta-learner, which is a lightweight tree-based ensemble. The inference time for the full-year test set is less than one minute, while smaller seasonal, weekday, and weekend subsets typically require only several seconds.

Overall, the runtime scales primarily with two factors: the number of time-series samples and the number of selected base models within each tier. The tiered model-selection strategy further mitigates computational overhead by avoiding unnecessary model complexity for stable datasets, thereby reducing the number of models that must be trained for less volatile data partitions.

- Practical implications

These results demonstrate that the main computational cost is associated with offline training, which is performed once during model development. In contrast, online prediction and dispatch support, which are critical for real-time BSMG operation, remain computationally efficient, with inference times well within the requirements of operational forecasting systems. The proposed framework is therefore scalable and practically deployable across a wide range of dataset sizes and application scenarios.

5) Online deployment and scheduling-interval scope

A clear distinction must be drawn between offline training time and online execution time when evaluating the practical deployability of the proposed framework. The runtime of "several tens of minutes" reported earlier refers to the complete offline workflow, which encompasses dataset stability assessment, training of the first-level base models, and RF meta-learner training. These operations are carried out during model development or periodic updating and are not repeated at every dispatch interval [60].

During online deployment, the trained forecasting models are applied directly for prediction, followed by communication-link availability updating and dispatch optimization. In the single-interval online test, forecast generation and communication-link availability updating require approximately 0.4 s and 0.3 s, respectively, while dispatch optimization dominates the remaining runtime at approximately 2.5–3.3 s. The overall online execution time is therefore approximately 3–4 s per dispatch interval.

Taking the conservative upper bound of 4 s, the online execution time represents roughly 0.11%, 0.44%, and 1.33% of 1-h, 15-min, and 5-min scheduling intervals, respectively. Consequently, the measured runtime offers sufficient computational margin for the hourly scheduling adopted in this study and remains well below the shorter 15-min and 5-min decision intervals under the tested system scale.

For more demanding near-real-time applications with substantially shorter decision intervals or larger system scales, further acceleration may be necessary, as online mixed-integer optimization can become computationally expensive under tight timing constraints [61], [62]. Potential strategies to address this challenge include:

- Lightweight model pools with fewer base models for faster inference.
- Incremental updating of models rather than full retraining.
- Parallel computation to distribute the computational burden.
- Approximate optimization methods to accelerate the dispatch solution.

These extensions are beyond the current scope of this study and are identified as important directions for future work.

J. Assumptions, Limitations, and Future Work

The proposed framework is developed under several modeling assumptions. First, the dataset evaluation stage assumes that the five selected indicators, namely ADF, SS, ApEn, H, and TRVR, can jointly provide a sufficiently informative characterization of dataset stability, periodicity, and complexity for model-tier selection. Second, the tiered forecasting strategy assumes that the predefined mapping from dataset score to model complexity is appropriate for the considered BSMG scenarios. Third, the operational scheduling model assumes that the system parameters, including battery limits, charging and discharging efficiency, and power balance constraints, are accurately known and remain valid throughout the scheduling horizon. Fourth, the communication-failure analysis assumes that link outages mainly affect information exchange and trading coordination, and that alternative transactions with the main grid or remaining BSMGs can still be executed once the original communication path is unavailable. Finally, because historical P2P transaction records among BSMGs are difficult to obtain, the internal trading data are synthetically generated from economic dispatch results with truncated Gaussian perturbations, which are assumed to reasonably approximate practical trading variability.

Despite the encouraging results, several limitations should be acknowledged. Since the proposed method is validated through simulation rather than hardware-in-the-loop or field deployment, its performance under strict latency-constrained near-real-time dispatch remains to be further verified. In addition, although the synthetic trading records are designed to reflect plausible internal exchange behaviors, they cannot fully reproduce all operational uncertainties, strategic interactions, and market frictions present in real P2P energy trading environments. The communication-unavailability scenarios considered in this study mainly represent constrained information exchange and reallocation of trading decisions, but do not capture detailed packet-level communication dynamics, delay accumulation, cyber-attacks, partial observability, or recovery processes. Moreover, the current tier boundaries and model pool are defined empirically for the studied datasets, and their direct transferability to other microgrid scales, market settings, or climatic regions may require recalibration. The present framework also focuses on hourly scheduling and forecasting, which may not fully capture faster operational dynamics in highly volatile systems.

Accordingly, future work will focus on three directions. First, the framework will be tested on real multi-BS microgrid platforms or hardware-in-the-loop environments to validate its practical robustness and deployment feasibility. Second, more comprehensive communication uncertainty models, including delay, packet disorder, partial link degradation, and cyber-physical disturbances, will be incorporated into the forecasting-dispatch loop. Third, the current deterministic forecasting and tier-selection mechanism will be extended toward uncertainty-

aware and online adaptive formulations, such as probabilistic forecasting, dynamic model-pool updating, and real-time fault-resilient energy trading for larger-scale BSMG networks.

VI. CONCLUSION

This paper addressed a critical but often overlooked challenge in cellular BSMG operation, namely the forecasting model performance depends heavily on the underlying stability characteristics of historical datasets, yet no systematic framework exists to assess data stability or to guide model selection accordingly. This problem is exacerbated by communication link failures, which disrupt data exchange and increase transaction costs. To tackle this, the paper proposed a stability-guided stacked-ensemble forecasting framework that integrates dataset characterization, multi-criteria stability ranking, selective model assembly, and RF-Stacking-based fusion to enhance both forecast accuracy and operational resilience.

The study applies five complementary metrics, including ADF test, SS, ApEn, H, and TRVR, to fully characterize each dataset. An enhanced GRA method (integrating EWM, CRITIC, and TF-AHP) then ranks stability and determines both the types and numbers of base models, improving accuracy while maintaining low complexity. The base model pool comprises three statistical methods, three ML algorithms, two DL architectures, and two RL techniques. The RF stacking model integrates their outputs, handles noisy high-dimensional data, captures nonlinear relationships, and reduces tuning requirements. A unified cost model compares energy-trading expenses under normal operation and under two-station and three-station communication failures across different datasets. Simulations validate the approach and yield the following conclusions:

1) Stability-guided model selection improves forecast accuracy. By assessing dataset stability with all five metrics and selecting model complexity accordingly, the weekday median RMSE is reduced from 0.32 to 0.27 (approximately 18.5% reduction), and the median R^2 increases from 0.59 to 0.71 (approximately 16.9% improvement). In contrast, relying on only three metrics misclassifies stability, leads to inappropriate model selection, and consequently degrades forecast accuracy.

2) The enhanced GRA corrects stability misclassifications. Integrating EWM, CRITIC, and TF-AHP into GRA improves dataset evaluation by correcting misclassifications observed with the original GRA. This is illustrated by the reassignment of the weekday dataset from T1 to T2, and the all-days dataset from T2 to T1, enabling more appropriate model selection that reflects the true stability characteristics of the data.

3) The tiered RF-Stacking ensemble consistently outperforms single models. Comparing normalized RMSE and R^2 across temporal partitions confirms that the proposed approach consistently enhances forecast performance, achieving 14–53% lower RMSE and 3–20% higher R^2 than the best-performing single models. This demonstrates superior robustness, generalization, and adaptability to varying dataset stability conditions.

4) Improved forecasting directly mitigates economic impacts of communication failures. Across two-link and three-link disruption scenarios, RF-Stacking-enabled dispatch reduces fault-induced transaction cost increases by approximately 15% and up to 40%, respectively. This highlights the resilience benefits of accurate forecasting under network faults and confirms the suitability of the proposed stability-guided stacked-ensemble framework for communication-constrained operational environments.

In summary, this paper demonstrates that systematically linking data stability assessment to ensemble model selection, rather than applying a fixed forecasting architecture, provides a practical and effective pathway toward resilient and economical BSMG operation, particularly when communication failures threaten real-time data availability.

REFERENCES

[1] J. Han, Y. Fang, E. Du, P. Yong, N. Zhang, and N. Liu, "Eliminating Distribution Network Congestion Based on Spatial-Temporal Migration of Multiple Base Stations," *IEEE Trans. Smart Grid*, vol. 15, no. 8, pp. 1234–1245, 2024.

[2] P. Gorla, M. Saif, V. Chamola, B. Sikdar, and M. Guizani, "Decentralized Renewable Resource Redistribution and Optimization for Beyond 5G Small Cell Base Stations: A Machine Learning Approach," *IEEE Syst. J.*, vol. 17, no. 1, pp. 988–999, Mar. 2023.

[3] M. Abuyaghi, S. Si-Mohammed, G. Shaker, and C. Rosenberg, "Positioning in 5G Networks: Emerging Techniques, Use Cases, and Challenges," *IEEE Internet Things J.*, vol. 12, no. 2, pp. 1408–1427, Jan. 2025.

[4] T. Liu, S. Zhang, X. Qu, L. Yang, C. Li, and Y. Chen, "Joint Optimization for IRS-Assisted Self-Powered IoT in 5G mmWave Networks,'" *IEEE Trans. Mobile Comput.*, vol. 24, no. 8, pp. 7092–7106, Aug. 2025.

[5] B. Zeng, W. Zhang, P. Hu, J. Sun, and D. Gong, "Synergetic Renewable Generation Allocation and 5G Base Station Placement for Decarbonizing Development of Power Distribution System: A Multi-objective Interval Evolutionary Optimization Approach," *Appl. Energy*, vol. 351, pp. 121831, Dec. 2023.

[6] J. Hu, L. Xia, J. Hu, and H. Wu, "Economical and Reliable Energy Management for Networked Microgrids in a Multi-Agent Collaborative Manner," *IEEE Trans. Autom. Sci. Eng.*, vol. 22, pp. 8659–8669, Nov. 2024.

[7] O. A. Talab and I. Avci, "Energy Management in Microgrids Using Model-Free Deep Reinforcement Learning Approach," *IEEE Access*, vol. 13, pp. 5871–5891, Jan. 2025.

[8] Z. Huang, K.-W. Lao, S. Yang, G. Feng, J. Gong, N. Lin, and Y. Nie, "Enhancing the Self-Healing Capability of Cyber-Physical Distribution Systems: An AAV-5G Hybrid Wired/Wireless Communication Method," *IEEE Trans. Smart Grid*, vol. 16, no. 4, pp. 3445–3448, Jan. 2025.

[9] J. Zhong, C. Chen, Z. Bie, and M. Shahidehpour, "Strategic SDN-Based Microgrid Formation for Managing Communication Failures in Distribution System Restoration," *IEEE Trans. Power Syst.*, vol. 40, no. 3, pp. 2506–2518, May 2025.

[10] N. S. Shibu, A. R. Devidas, S. Balamurugan, S. Ponnekanti, and M. V. Ramesh, "Optimizing Microgrid Resilience: Integrating IoT, Blockchain, and Smart Contracts for Power Outage Management," *IEEE Access*, vol. 12, pp. 18782–18803, Jan. 2024.

[11] H. Zhang, C. Chen, J. Zhong, Z. Bie, and G. Liu, "A Joint Communication-Load Restoration Strategy Based on UAVs for Resilient Distribution System," *IEEE Trans. Power Syst.*, Jun. 25, 2025.

[12] M. Yan, T. Qin, W. Guo, and Y. Hu, "Cooperative Sleep and Energy-Sharing Strategy for a Heterogeneous 5G Base Station Microgrid System Integrated with Deep Learning and an Improved MOEA/D Algorithm," *Energies*, vol. 18, no. 7, pp. 1580, Mar. 2025.

[13] A. Zohaib, F. Akram, S. Khalid, H. Nawaz, and M. U. Rehman, "Hybrid Deep Learning Based Load Forecasting and AI-Driven Energy Management for Grid-Connected Multi-Microgrids," *Computers and Electrical Engineering*, vol. 131, pp. 110915, Mar. 2026.

[14] H. Wang, J. Ge, Y. Zhao, J. Gu, C. Li, and C. Liu, "Resilience Enhancement Strategies for Distribution Networks Considering the Coordination of 5G Base Stations and Multiple Flexible Resources," *Scientific Reports*, Jan. 2026.

[15] Y. Qiao, W. Li, and D. Guo, "AI-Enhanced Model Predictive Control in Microgrids: Systematic Review of Algorithms, Applications, and Emerging Trends," *J. Power Electron.*, pp. 1–12, Feb. 2026.

[16]Z. P. Yuan, P. Li, Z. L. Li, and J. Xia, "A Fully Distributed Privacy-Preserving Energy Management System for Networked Microgrid Cluster Based on Homomorphic Encryption," *IEEE Trans. Smart Grid*, vol. 15, no. 2, pp. 1735–1748, Aug. 2023.

[17]Y. Lv, Z. Wu, and X. Zhao, "Data-Based Optimal Microgrid Management for Energy Trading with Integral Q-Learning Scheme," *IEEE Internet Things J.*, vol. 10, no. 18, pp. 16183–16193, Apr. 2023.

[18]L. S. Chaves, J. M. S. Callegari, L. S. Araujo, and D. I. Brandao, "Impact of Latency and Packet Error on Communication in Centralized Microgrid Control: Modeling and Guidelines," *IEEE Access*, May 2025.

[19]M. Yan, W. Guo, H. Zheng, and T. Qin, "NTP-MAPPO and SDN for Energy Trading Among Multi-Base-Station Microgrids," *IEEE Internet Things J.*, vol. 11, no. 10, pp. 18568–18579, Feb. 2024.

[20]P. Bao, Q. Xu, Y. Yang, and X. Zhao, "Cooperative Game-Based Solution for Power System Dynamic Economic Dispatch Considering Uncertainties: A Case Study of Large-Scale 5G Base Stations as Virtual Power Plant," *Appl. Energy*, vol. 368, pp. 123463, Aug. 2024.

[21]S. S. Surathunmanun, W. Ongsakul, J. G. Singh, and K. Mehran, "Short-term Solar PV Forecasting in Microgrids Using Cloud Top Temperature and Vision Transformer Based Models," *Front. Energy Res.*, vol. 13, pp. 1691881, Jan. 2025.

[22]H. Zhou, A. Aral, I. Brandić, and M. Erol-Kantarci, "Multiagent Bayesian Deep Reinforcement Learning for Microgrid Energy Management Under Communication Failures," *IEEE Internet Things J.*, vol. 9, no. 14, pp. 11685–11698, July 2022.

[23]B. Arbab-Zavar, S.M. Sharkh, E.J. Palacios-Garcia, J.C. Vasquez, and J.M. Guerrero, "Reducing Detrimental Communication Failure Impacts in Microgrids by Using Deep Learning Techniques," *Sensors*, vol. 22, no. 16, pp. 6006, Aug 2022.

[24]N. Zhang, D. Liu, T. Liu, X. Zhang, J. Guo, F. Lan, Q. Li, W. Lu, and X. Yang, "A Win-Win Coordinated Scheduling Strategy Between Flexible Load Resource Operators and Smart Grid in 5G Era," *Energies*, vol. 18, no. 6, pp. 1510, Mar. 2025.

[25]S. M. Rahmatinia, S.-M. Hosseini, and S.-A. Hosseini-Seno, "CLM-Former for Enhancing Multi-Horizon Time Series Forecasting and Load Prediction in Smart Microgrids Using a Robust Transformer-Based Model," *Sci. Rep.*, vol. 16, no. 4704, Jan. 2026.

[26]Z. Peng, H. Han, and J. Ma, "IAVOA–EATCN: An Adaptive Deep Framework for Accurate Power Load Forecasting," *Symmetry,* vol. 18, no. 1, pp. 102, Jan. 2026.

[27]H. Qiu, R. Hu, J. Chen, and Z. Yuan, "Short-Term Electricity Load Forecasting Based on Complete Ensemble Empirical Mode Decomposition with Adaptive Noise and Improved Sparrow Search Algorithm–Convolutional Neural Network–Bidirectional Long Short-Term Memory Model," *Mathematics*, vol. 13, no. 5, no. 813, Feb. 2025.

[28]Y. Chen, J. Qiu, Y. Lu, and L. Jiao, "Real-World Short-Term Load Forecasting Using a Dual-Channel Multi-Scale LSTM with Wavelet Decomposition and Cross-Channel Attention," Discover Electronics, vol. 3, no. 1, pp. 83, Jun. 2026.

[29]K. Bandara, R.J. Hyndman, and C. Bergmeir, "MSTL: A Seasonal-Trend Decomposition Algorithm for Time Series with Multiple Seasonal Patterns," *Int. J. Oper. Res.*, Jan. 2025.

[30]E. Paparoditis and D.N. Politis, "The Asymptotic Size and Power of the Augmented Dickey–Fuller Test for a Unit Root," *Econom. Rev.*, vol. 37, no. 9, pp. 955–973, Oct. 2018.

[31]R. J. Hyndman and G. Athanasopoulos, "Forecasting: Principles and Practice," *OTexts*, 2018.

[32]J. M. Yentes, N. Hunt, K. K. Schmid, J. P. Kaipust, D. McGrath, and N. Stergiou, "The Appropriate Use of Approximate Entropy and Sample Entropy with Short Data Sets," *Ann. Biomed. Eng.*, vol. 41, no. 2, pp. 349–365, Feb. 2013.

[33]J. B. Florindo, R. R. Lima, F. A. dos Santos, and J. L. Alves, "GHENet: Attention-based Hurst Exponents for the Forecasting of Stock Market Indexes," *Physica A*, vol. 667, no. 130540, Jun. 2025.

[34]L. H. Dicker, "Residual Variance and the Signal-to-Noise Ratio in High-Dimensional Linear Models," *arXiv preprint arXiv:1209.0012*, Aug. 2012.

[35]Y. Liu, C. M. Eckert, and C. Earl, "A Review of Fuzzy AHP Methods for Decision-Making with Subjective Judgements," *Expert Syst. Appl.*, vol. 161, pp. 113738, Dec. 2020.

[36]A. M. Hagag, L. S. Yousef, and T. F. Abdelmaguid, "Multi-Criteria Decision-Making for Machine Selection in Manufacturing and Construction: Recent Trends," *Mathematics*, vol. 11, no. 3, pp. 631, 2023.

[37]R. Kumar, S. Singh, P. S. Bilga, J. Singh, S. Singh, M. L. Scutaru, and C. I. Pruncu, "Revealing the Benefits of Entropy Weights Method for Multi-Objective Optimization in Machining Operations: A Critical Review," *J. Mater. Res. Technol.*, vol. 10, pp. 1471–1492, Jan. 2021.

[38]W. Zhang, X. Zhang, F. Liu, Y. Huang, and Y. Xie, "Evaluation of the Urban Low-Carbon Sustainable Development Capability Based on the TOPSIS-BP Neural Network and Grey Relational Analysis," *Complexity*, vol. 2020, no. 1, pp. 6616988, 2020.

[39]Y. Wu, Y. Ma, and H. Aliev, "A Novel Reinforcement Learning-Based Approach for Short-Term Load and Price Forecasting in Energy Markets," *Sci. Rep.*, Jan. 2026.

[40]N. Ali, R. Shaw, and K. Mason, "Forecast aware deep reinforcement learning for efficient electricity load scheduling in dairy farms," *arXiv preprint arXiv:2601.08052*, 2026.

[41]D. Kumar and A. Kumar, "A Reliable Hybrid Autoregressive Integrated Moving Average and Deep Reinforcement Machine Learning Strategy for Resiliency Enhancement in Microgrid," *Sustain. Energy, Grids and Networks*, vol. 39, no. 101424, Sep. 2024.

[42]M. Mohamed, F. E. Mahmood, M. A. Abd, A. Chandra, and B. Singh, "Dynamic Forecasting of Solar Energy Microgrid Systems Using Feature Engineering," *IEEE Trans. Ind. Appl.*, vol. 58, no. 6, pp. 7857–7869, Aug. 2022.

[43]S. O. G. Torto, R. K. Pachauri, and J. G. Singh, "Neural Prophet Driven Day-ahead Forecast of Global Horizontal Irradiance for Efficient Micro-grid Management," *e-Prime–Advances in Electrical Engineering, Electronics and Energy*, vol. 10, no. 100817, Dec. 2024.

[44]Z. Qinghe, X. Wen, H. Boyan, W. Jong, and F. Junlong, "Optimised Extreme Gradient Boosting Model for Short Term Electric Load Demand Forecasting of Regional Grid System," *Sci. Rep.*, vol. 12, no. 1, pp. 19282, Nov. 2022.

[45]J. Guo, S. Yun, Y. Meng, N. He, D. Ye, Z. Zhao, L. Jia, and L. Yang, "Prediction of Heating and Cooling Loads Based on Light Gradient Boosting Machine Algorithms," *Build. Environ.*, vol. 236, pp. 110252, May 2023.

[46]W. Yan and J. Zhang, "Improving Short-Term Active Power Prediction Through Optimization of the Categorical Boosting Model with Meta-Heuristic Algorithms," *Electr. Eng.*, vol. 30, pp. 1–22, Dec. 2024.

[47]S. A. Alavi, K. Mehran, V. Vahidinasab, and J. P. S. Catalão, "Forecast-Based Consensus Control for DC Microgrids Using Distributed Long Short-Term Memory Deep Learning Models," *IEEE Trans. Smart Grid*, vol. 12, no. 5, pp. 3718–3730, Apr. 2021.

[48]J. Wu, Z. Chang, L. Zhang, M. Chen, S. Li, and F. Qiu, "A Dual-Branch Transformer Network with Multi-Scale Attention Mechanism for Microgrid Wind Turbine Power Forecasting," *Electronics*, vol. 14, no. 13, pp. 2566, Jun. 2025.

[49]H. Xiao, X. Pu, W. Pei, L. Ma, and T. Ma, "A Novel Energy Management Method for Networked Multi-Energy Microgrids Based on Improved DQN," *IEEE Trans. Smart Grid*, vol. 14, no. 6, pp. 4912–4926, Jun. 2023.

[50]D. Wang, Q. Sun, and H. Su, "Real-Time Optimal Energy Management of Microgrid Based on Multi-agent Proximal Policy Optimization," *Neural Comput. Appl.*, pp. 1–13, Feb. 2025.

[51]G. Muriithi and S. Chowdhury, "Deep Q-Network Application for Optimal Energy Management in a Grid-Tied Solar PV-Battery Microgrid," *J. Eng.*, vol. 2022, no. 4, pp. 422–441, Feb. 2022.

[52]Y. Sadeghpour, E. A. Farsani, H. R. Abdolmohammadi, and I. G. Sardou, "A Hybrid Transformer-PPO Framework for Multi-Objective Energy Management in Renewable-Based Microgrids," *Sci. Rep.*, vol. 16, no. 24645, May 2026.

[53]I. Serban, S. Cespedes, C. Marinescu, C. A. Azurdia-Meza, J. S. Gomez and D. S. Hueichapan, "Communication Requirements in Microgrids: A Practical Survey," *IEEE Access*, vol. 8, pp.47694-47712, Mar. 2020.

[54]A. R. Devidas and M. V. Ramesh, "Cost Optimal Hybrid Communication Model for Smart Distribution Grid," *IEEE Trans. Smart Grid*, vol. 13, no. 6, pp.4931-4942, Nov. 2022.

[55]A. M. Eltamaly and M. A. Ahmed, "Performance Evaluation of Communication Infrastructure for Peer-to-Peer Energy Trading in Community Microgrids," *Energies*, vol. 16, no. 13, pp. 5116, Jul. 2023.

[56]3GPP, "Service Requirements for Cyber-Physical Control Applications in Vertical Domains," 3GPP TS 22.104, ver. 18.4.0, Release 18, Jul. 2024.

[57]3GPP, "System Architecture for the 5G System (5GS)," 3GPP TS 23.501, ver. 18.5.0, Release 18, May 2024.

[58]I. Löser, A. K. Sampathirao, S. Hofmann, and J. Raisch, "Fallback Strategies in Operation Control of Microgrids with Communication Failures," *in Proc. IEEE 58th Conference on Decision and Control (CDC)*, Nice, France, pp. 3885–3891, Dec. 2019.

[59]X. Lai, S. Deng, L. Yu, Y. Lai, S. Qiao, and X. Zhang, "Rethinking Recurrent Neural Networks for Time Series Forecasting: A Reinforced Recurrent Encoder with Prediction-Oriented Proximal Policy Optimization," *Adv. Eng. Inform.*, vol. 76, no. 105047, Nov. 2026.
[60]V. Casagrande, M. Ferianc, M. Rodrigues, and F. Boem, "An Online Learning Method for Microgrid Energy Management Control," in *Proc. 31st Mediterranean Conf. Control Autom. (MED)*, Limassol, Cyprus, pp. 263–268, Jun. 2023.
[61] J. Hönen, J. L. Hurink, and B. Zwart, "Dynamic Rolling Horizon-Based Robust Energy Management for Microgrids Under Uncertainty," *arXiv preprint arXiv:2307.05154*, Jul. 2023.
[62]C. Liu, S. Shi, A. Alan, G. K. Venayagamoorthy, and B. De Schutter, "Approximate Model Predictive Control for Microgrid Energy Management via Imitation Learning," *arXiv preprint arXiv:2510.20040*, Apr. 2026.



Yingqi Zhu (Student Member, IEEE) received the B.Eng. degree in electrical engineering from North China University of Water Resources and Electric Power, Zhengzhou, China, in 2020, the M.Sc. degree in electrical engineering from University of Shanghai for Science and Technology, Shanghai, China, in 2023. She is currently working toward the Ph.D. degree in electronic and electrical engineering. Her research interests include base station microgrids energy management, energy trading, scheduling, and energy efficiency optimization.



Kang Li (Senior Member, IEEE) received the B.Sc. degree in industrial automation from Xiangtan University, Xiangtan, China, in 1989, the M.Sc. degree in control theory and applications from the Harbin Institute of Technology, Harbin, China, in 1992, and the Ph.D. degree in control theory and applications from Shanghai Jiaotong University, Shanghai, China, in 1995. He also received the D.Sc. degree in engineering from Queen's University Belfast, Belfast, U.K. in 2015. He currently holds the Chair of Smart Energy Systems at the University of Leeds, U.K. He has authored/co-authored more than 200 journal publications and edited/co-edited 18 conference proceedings, winning over 20 prizes and awards. His research interests include nonlinear system modeling, identification, control, and machine learning, with substantial applications in energy and power systems, transport decarbonization, and energy management in energy intensive manufacturing processes.



Li Zhang (Senior Member, IEEE) received the Ph.D. degree in communications from the University of York, York, U.K., in 2003. She is currently an Associate Professor and leads the Wireless Communication Group with the School of Electronic and Electrical Engineering, University of Leeds, Leeds, U.K. Her research interest includes wireless communications and signal processing techniques, such as massive MlMO, mm-Wave communications, heterogeneous networks, device to device communications. and 5G systems. Since 2006, she has been serving on the Technical Programme Committees of most major IEEE conferences in communications. She is an Associate Editor for the IEEE journal. In 2006, she became a Fellow of the Higher Education Academy. In 2011, she was the recipient of IEEE exemplary Reviewer. In 2012, she was promoted as senior IEEE Member.